Sensitivity Analysis of Wellbore Mud Pressure towards Anisotropic Shale Properties, Pore Fluid Pressure and Far Field Stresses

applied sciences

MDPI

Article

Sensitivity Analysis of Wellbore Mud Pressure towards Anisotropic Shale Properties, Pore Fluid Pressure and Far Field Stresses

Chiara Deangeli [1,*], Wenjie Liu [1,2] and Ke Yang [2]

[1] Department of Environment, Land and Infrastructure Engineering (DIATI), Politecnico di Torino, Corso Duca degli Abruzzi 24, 10129 Torino, Italy; wenjie.liu@polito.it
[2] Department of Mining Engineering, Anhui University of Science and Technology, Huainan 232001, China; keyang@aust.edu.cn
* Correspondence: chiara.deangeli@polito.it

Abstract: The paper investigates the mud pressure to maintain the stability of wellbores drilled in transversely isotropic shale through sensitivity analyses, carried out with analytical and numerical modeling (FLAC). To this end, we interpreted the anisotropic strength of the Tournemire shale with the Weakness Plane Model (WPM) and the modified Hoek–Brown criterion (HBm). The sensitivity analyses of synthetic case studies indicated a different trend in mud pressure for the two criteria. In some cases, the WPM predicts mud pressures higher than those predicted by the HBm and vice versa. The mud pressures predicted by the HBm resulted in being more sensitive to the increase in the anisotropy of the far field stresses for all the inclinations of the weakness planes. In this context, the WPM predicts some anomalous low mud pressures in a wide range of inclinations of the weak planes. The change in the frictional component of strength decreases with an increase in the pore fluid pressure for both criteria. The mud pressure predicted by the WPM resulted in being more sensitive to the change in frictional strength. The change in trend of the two criteria with change in input data suggests caution in the "a priori" selection of the strength criterion. A simple solution is proposed to predict a safe and reliable mud pressure with a small number of lab tests.

Keywords: transversely isotropic shale; Weakness Plane Model; Hoek–Brown criterion; analytical and numerical modeling; FLAC

Citation: Deangeli, C.; Liu, W.; Yang, K. Sensitivity Analysis of Wellbore Mud Pressure towards Anisotropic Shale Properties, Pore Fluid Pressure and Far Field Stresses. *Appl. Sci.* **2024**, *14*, 148. https://doi.org/10.3390/app14010148

Academic Editor: Nikolaos Koukouzas

Received: 13 November 2023
Revised: 10 December 2023
Accepted: 19 December 2023
Published: 23 December 2023

1. Introduction

Wellbores drilled in sedimentary basins encounter different rocks with different mechanical responses.

Shale makes up approximately 50 percent of all sedimentary rocks in the stratigraphic record [1], and the majority of deep drilling operations come across this rock [2]. In the oil and gas industry, more than 75% of the world drilling is carried out in shales, which are responsible for the major source (90%) of instability [3].

Currently, the mitigation of the effects of anthropogenic greenhouse gas emissions should lead to oil and gas output being in gradual decline. However, depleted oil and gas fields are good targets for CO_2 and H_2 storage [4–7]. In these depleted fields, new wellbores must be drilled for gas injection operations. Consequently, drilling operation in shale is still a matter of concern [8–17].

The prediction of the mud pressure to avoid wellbore instability requires the knowledge of the mechanical properties of the rock. The determination of the shale mechanical properties at large depth is still a problem. An accurate assessment of rock mechanical properties is through laboratory tests; however, core retrieval at large depths can be a difficult task [18]. In fact, shale cores can be subject to alteration as they are retrieved

from the subsurface due to changes in pressure, temperature and oxidation state [19]. Furthermore, the processes of specimen preparation can induce damage [20]. All these problems can make the results of tests uncertain. As the process of rock coring can damage the material, the mechanical properties can be obtained from laboratory tests carried out on outcropping formations with structures close to the rock at a large depth [21]. The laboratory tests for the geomechanical characterization of shales with anisotropic strength consists of uniaxial and triaxial tests carried out at five or more inclinations of the weakness planes. The tests should be repeated at least twice for each inclination of the weakness planes, to verify their reliability. Therefore, the extensive process of coring and testing can result in being expensive and time consuming.

More often, the mechanical properties of the rock at large depths are obtained from indirect measurements by using correlations with log data and microscopic models [22,23]. These empirical correlations are used to obtain a continuous profile with the depth of the elastic and strength properties [24] and, for a given wellbore, log-derived data, are correlated with the rock properties measured in laboratory. In general, the empirical relationships with log data are valid in the basin from where they were set up. A thorough review of published empirical relations is given in [25,26]. Furthermore, [27] presented new correlations for deep-water reservoirs and shale oil and shale gas formations.

Recently, the Machine Learning Approach and hybrid neural net based models were proposed for the indirect determination of the uniaxial compressive strength and internal friction angle of shale [28,29].

According to [22–24,30], the mechanical properties obtained by log and microscopic models are affected by relevant uncertainty and cannot provide a thoroughgoing characterization of the rock. Shale often exhibits variation in strength properties along and across the lamination planes. This variation must be taken into consideration when carrying out stability analyses of wellbores [17]. However, the transverse isotropy of shale is not specifically addressed in the indirect approaches.

The effect of water weakening in a variety of sedimentary rocks has been widely investigated (i.e., [17,31–35]). On the other hand, the low permeability of shale rock can induce undrained conditions, immediately after drilling (short term). The undrained pore fluid pressure evolution can enhance plasticity [36–39].

In this study, we investigated the mud pressure to maintain the stability of wellbores drilled in transversely isotropic shale through sensitivity analyses. These analyses were carried out with analytical and numerical modeling (FLAC 2D, ver.8.1, Itasca, IL, USA). We determined the strength properties of the Tournemire shale from the regressions of the data of lab tests carried out by [40] with the Weakness Plane Model [41] (WPM) and the Hoek–Brown criterion (HB) [42,43] adapted to anisotropic rock (HBm). We performed sensitivity analyses of synthetic cases by varying the inclination of the weakness planes, the far field stress anisotropy, the pore fluid pressure and the frictional component of the rock strength.

The results of these analyses identified the pros and cons of the predictions of WPM and HBm. Finally, we propose a simple solution for predicting a safe and reliable mud pressure with a small number of lab tests.

The flowchart of this study is reported in Figure 1.

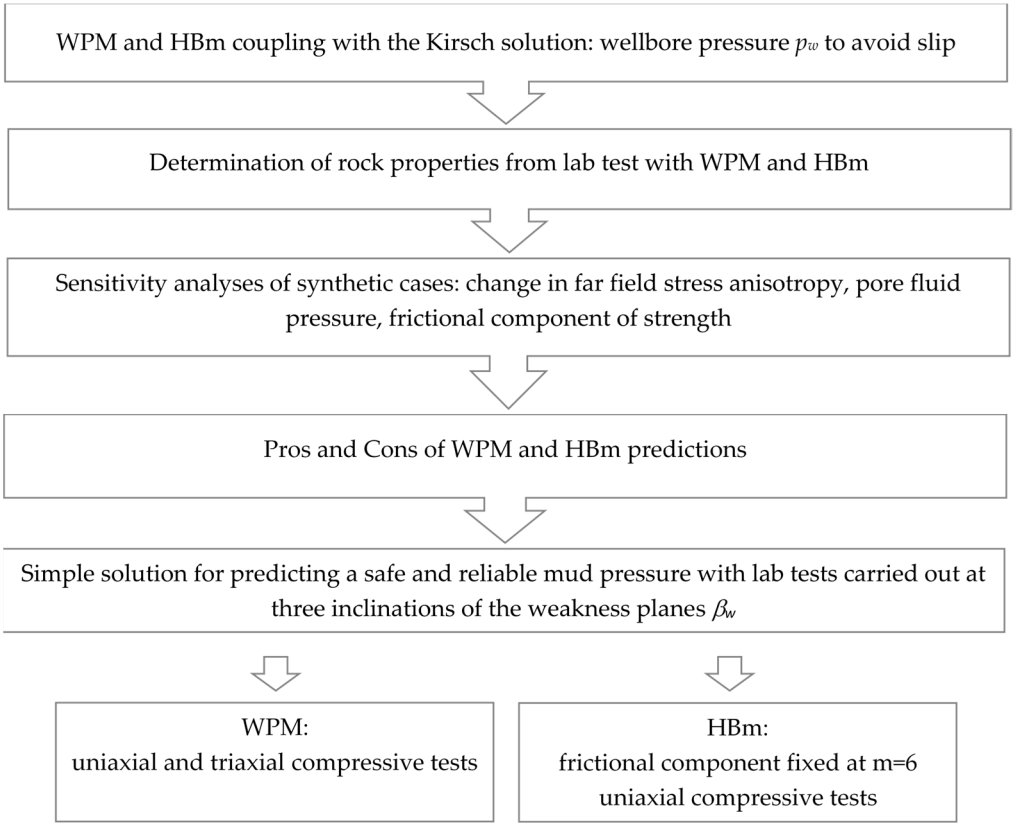

Figure 1. Flowchart of the study.

2. Materials and Methods

This section presents the strength criteria for isotropic and transversely isotropic rocks and the related mud pressure formulas for avoiding shear failure.

2.1. *Strength Criteria*

Sedimentary rocks are porous materials and can exhibit a significant strength decrease with the increase in the pore water pressure. Consequently, the pore water pressure must be taken into account in the mechanical analysis. The concept of effective stress was originally introduced by Terzaghi [44] for soils. According to [45], the theory of poroelasticity demonstrates that the deformation of the porous material is proportional to the effective stress:

$$\sigma'_{ij} = \sigma_{ij} - \alpha p_f \delta_{ij}, \quad (1)$$

where: σ'_{ij} and σ_{ij} are the effective and total stress tensors, respectively; α is the Biot coefficient, function of the bulk moduli of the rock skeleton, rock grains and fluid; p_f is the pore pressure in the porous medium; δ_{ij} is the Kronecker function.

Equation (1) assumes that the rock is linearly elastic. This assumption is not directly applicable to rocks subject to failure processes [46]. The Terzaghi's principle of effective stress for soils ($\alpha = 1$) seems to be the most appropriate definition to be used in rock failure analysis [46,47].

All the subsequent analyses are carried out with the effective stresses. The deviatoric stress ($\sigma_1 - \sigma_3$) is reported in terms of total stresses, because it is always an effective stress: $[\sigma_1 - \sigma_3] = [(\sigma_1 - p_f) - (\sigma_3 - p_f)] = [\sigma'_1 - \sigma'_3]$.

Rock failure is generally approached in terms of isotropic behavior; however, the actual behavior of many rocks is anisotropic. Shales are frequently affected by parallel

weakness planes, with reduced strength compared to intact material. The analysis of failure in such rocks needs a strength criterion which accounts for the strength anisotropy.

The most widely used criterion is WPM, that considers a set of parallel discontinuities on which failure occurs in the form of slip. WPM written in terms of principal stresses (σ_1 and σ_3) becomes

$$\left(\sigma_1-\sigma_3\right)_{slip}=\frac{2\left(c'_w+\sigma'_3\tan\phi'_w\right)}{\left(1-\frac{\tan\phi'_w}{\tan\beta_w}\right)\sin 2\beta_w} \tag{2a}$$

where β_w, c'_w and ϕ'_w are the inclination, the cohesion and the friction angle of the weakness planes, respectively.

Figure 2 shows the plot of Equation (2a): the minimum strength occurs at $\beta_w = 45° + \phi'_w/2$ and for values of β_w, close to 90° and in the range 0°-ϕ'_w, slip on the plane of weakness cannot occur. Within these ranges, shear failure occurs through the rock material in a direction not controlled by the plane of weakness [47]. The plateau of constant strength represents the resistance of the rock in the ranges of β_w that are not predicted by Equation (2a). The plateau of constant strength can be described by the Mohr–Coulomb criterion (M-C):

$$\sigma'_1=\frac{2c'\cos\phi'}{\left(1-\sin\phi'\right)}+\sigma'_3\frac{\left(1+\sin\phi'\right)}{\left(1-\sin\phi'\right)}=\sigma_c+\sigma'_3N_\phi\,, \tag{2b}$$

where c' is the cohesion, ϕ' is the friction angle, σ_c is the uniaxial compressive strength of the intact rock and N_ϕ is the slope of the strength envelope.

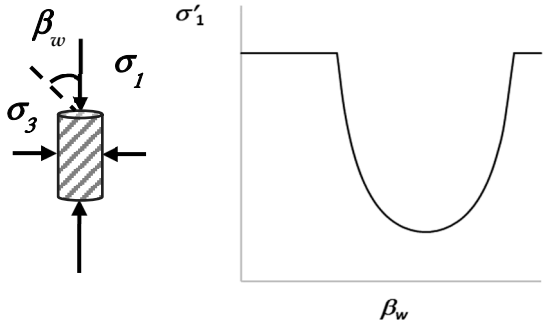

Figure 2. Trend of the strength with β_w in the Weakness Plane Model (WPM).

WPM needs the calculation of the strength with Equations (2a) and (2b) for a given β_w. The equation that predicts the lowest strength must be considered for failure. WPM is a simple criterion that does not take into account the contemporary development of slip and failure in the intact rock, observed in laboratory tests [48]. Furthermore, the plateau of constant strength is not always observed in the experimental tests.

The use of WPM needs the determination of the cohesion c'_w and the friction angle ϕ'_w of the weakness planes and the cohesion c' and the friction angle ϕ' of the rock matrix (plateau strength).

HB was specifically proposed for intact rock and rock masses and is widely used for a variety of rock engineering problems [42,43]. There are different versions of HBm adapted to transversely isotropic rocks (i.e., [48–51]). In this modified criterion, there is no distinction between failure along the weakness planes and failure in the rock matrix. A single continuous function describes the criterion.

Refs. [50,51] assumed that the rock is intact (s = 1), and the uniaxial compressive strength and the empirical dimensionless constants vary at every inclination β_w of the weakness planes (instantaneous isotropy). Under these conditions, HBm becomes

$$\left(\sigma_1-\sigma_3\right)_{\beta w}=\left(m_{\beta w}\sigma_{c\beta w}\sigma_3'+\sigma_{c\beta w}^2\right)^{0.5} \quad (3)$$

where $\sigma_{c\beta w}$ and $m_{\beta w}$ are the instantaneous uniaxial compressive strength of the rock and the instantaneous empirical dimensionless constant.

Figure 3a shows the strength envelops of a shale rock for different β_w. Equation (3) requires a high number of uniaxial/triaxial tests, for the determination of the strength parameters $\sigma_{c\beta w}$ and $m_{\beta w}$ at various inclinations of the weakness planes.

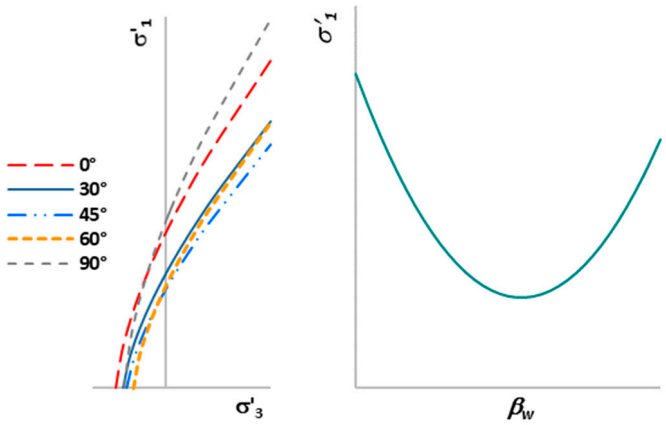

Figure 3. (**a**) Strength envelops of the Hoek–Brown criterion adapted to anisotropic rock (HBm) for different β_w. (**b**) Trend of the shale strength with β_w obtained with HBm.

HBm generally matches the results of compression tests quite well, compared to WPM. The variation of the strength with β_w can assume different trends [52–54] and is not constrained by both the minimum at $\beta_w = 45° + \phi'_w/2$ and the plateau of constant strength. Figure 2b shows a typical interpolating function of this variation.

Finally, the prediction of the uniaxial tensile strength with WPM and HBm is affected by the overestimation of this property [52]. A thorough review of the strength criteria for the prediction of the uniaxial tensile strength in transversely isotropic rocks was presented by [55–57].

2.2. Calculation of the Mud Pressure

The calculation of the mud pressure of a wellbore, drilled along a principal direction, requires the Kirsch solution coupled with the strength criteria described in Section 2.1.

At the boundary of the hole, the Kirsch solution in plane strain conditions (Figure 4) becomes

$$\begin{gathered}\sigma_\vartheta'=S-p_w-p_f,\\ \sigma_r'=p_w-p_f,\\ \sigma_{axis}'=S_z-p_f,\\ S=\sigma_{MAX}+\sigma_{min}-2\left(\sigma_{MAX}-\sigma_{min}\right)cos2\vartheta,\\ S_z=\sigma_z-2\nu\left(\sigma_{MAX}-\sigma_{\min}\right)\cos 2\vartheta\end{gathered} \quad (4)$$

where σ_{min}, σ_{MAX} and σ_z are the far field stresses, S and S_z are the induced state of stress, ϑ is the borehole azimuth, p_w is the mud pressure and ν is the Poisson ratio.

The analysis focuses on the combination of the effective tangential stress σ'_{ϑ} and radial stress σ'_r which are both affected by the mud pressure p_w (we disregarded the occurrence of failure with σ'_{axis}): $\sigma_\theta > \sigma_{axis} > \sigma_r$.

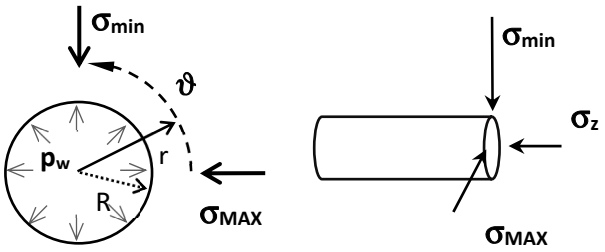

Figure 4. Variables reported in Equation (4): σ_{MAX}, σ_{min} and σ_z are the far field stresses; ϑ is the borehole azimuth and is counted from σ_{MAX}. R_w is the borehole radius and r is the radial distance; p_w is the mud pressure.

The coupling between Equation (4) and WPM (Equations (2a) and (2b)) gives the limit mud pressures for the weakness planes and the rock material:

$$p_{w\_slip} = \frac{S\left(1-\frac{\tan\phi'_w}{\tan\beta_w}\right)\sin 2\beta_w - 2c'_w + 2\tan\phi'_w p_f}{2\left[\tan\phi'_w + \left(1-\frac{\tan\phi'_w}{\tan\beta_w}\right)\sin 2\beta_w\right]}, \quad (5a)$$

$$p_{w\_MC} = \frac{S-\sigma_c + p_f(N_\phi - 1)}{\left(N_\phi + 1\right)} \quad (5b)$$

The coupling between Equation (4) and HBm gives [52]:

$$p_{w\_H\&Bm} = \frac{4S + m_{\beta w}\sigma_{c\beta w} - \left[\sigma^2_{c\beta w}(m^2_{\beta w}+16) + 8m_{\beta w}\sigma_{c\beta w}\left(S-2p_f\right)\right]^{0.5}}{8} \quad (6)$$

The angle β_w must be determined at any azimuth ϑ of the wellbore because it is one of the variables of Equation (5a) and is indirectly involved in Equation (6) for the calculation of the uniaxial compressive strength $\sigma_{c\beta w}$ and the dimensionless constant $m_{\beta w}$. The authors of [52] found the equations that relate to β_w, the inclination of the weakness plane δ and the azimuth ϑ. Figure 5 shows the change in the angle β_w with the inclination of the weakness plane δ, at different azimuth ϑ.

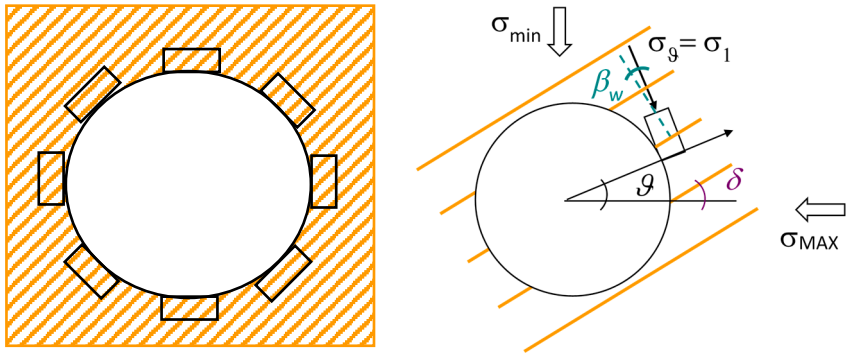

(**a**)

$$\beta_w = |\vartheta - \delta| \quad 0° \le \vartheta \le \delta + 90°$$

$$\beta_w = 180° - |\vartheta - \delta| \quad \delta + 90° \le \vartheta \le 180°$$

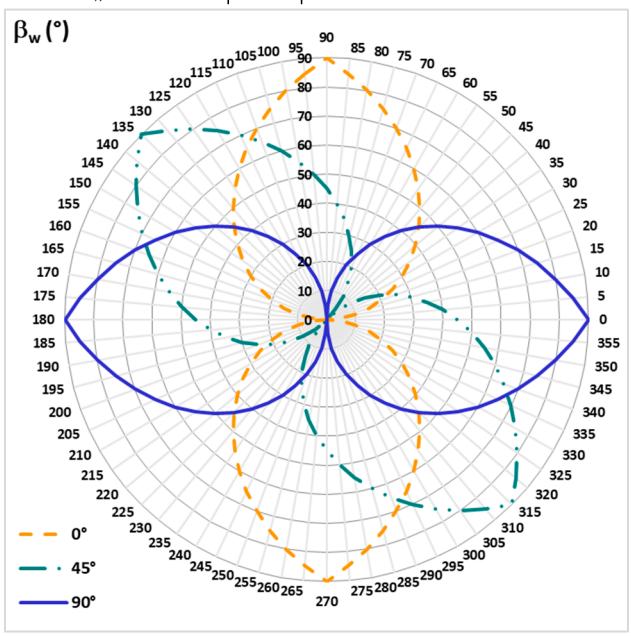

(**b**)

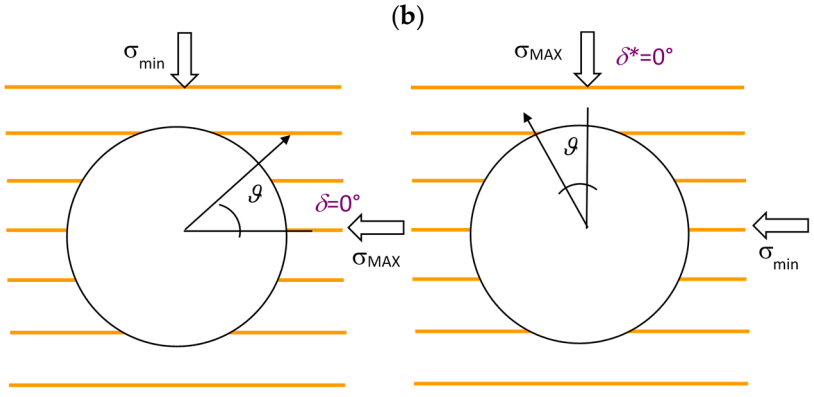

(**c**)

Figure 5. (**a**) Sketch of a wellbore drilled in rock with weakness planes. Definition of the angles δ, β_w and ϑ around the borehole. The continuous yellow lines are the weak planes. The dotted dark green line is the normal to the weak plane. The angle δ is measured counterclockwise from σ_{MAX}. The angle β_w is defined by the normal to the weak plane and the direction of the maximum principal stress (here $\sigma_\theta = \sigma_1$). (**b**) Formulas for the calculation of the angle β_w at any azimuth ϑ and plot of the trend of the angle β_w with ϑ for δ = 0°–45°–90° [52]. (**c**) Definition of δ^* = 0° from δ = 0°. Left: Reference system of Figure 5a for horizontal weakness planes δ = 0°. Right: Rotation of the far field stresses

with horizonal weakness planes $\delta^* = 0°$. The magnitude of the mud pressure for avoiding slip along the weakness planes is calculated at $\delta = 90°$ of the initial reference system.

Vertical weakness planes ($\delta = 90°$) seem to be uncommon in real fields [58]. Figure 5c shows horizontal weakness planes with the reference system shown in Figure 5a and with a rotation of the maximum and minimum far field stresses. This new configuration is equivalent to $\delta = 90°$ and is here defined as $\delta^* = 0°$. In this new system, the mud pressure for avoiding slip along the horizontal weakness planes must be calculated according to the case with $\delta = 90°$ of the original reference system (vertical planes).

The mud pressures reported in Equations (5) and (6) take into account the pore fluid pressure p_f, according to the Terzaghi principle (Equation (1)). Shales have a low permeability and immediately after drilling, the condition close to the boundary of the borehole can become undrained (no fluid flow through the rock pores). The undrained conditions can induce a change in pore fluid pressure $\Delta p_f \neq 0$ when $R > 1$ and the rock is soft. In other cases, there is no change in pore fluid pressure $\Delta p_f = 0$, with no fluid flow through the rock pores [59]. The evolution of the pore fluid pressure affects wellbore stability in the short term (undrained conditions) and in the long term (drained conditions).

3. Interpretation of Laboratory Tests on Tournemire Shale

The set-up of sensitivity analyses of wellbore stability requires the knowledge of the strength parameters. To this end, we interpreted laboratory tests carried out on Tournemire shale by [40].

3.1. *Determination of the Strength Properties with WPM and HBm*

Abdi et al. (2015) [40] carried out uniaxial, triaxial and Brazilian tests on Tournemire shale specimens at different inclinations of β_w of the weakness planes.

The strength parameters, necessary for the calculation of the mud pressures, are obtained with the regression of the data of these lab tests with WPM and HBm. We reduced the tensile strength of the Brazilian tests by a factor equal to 0.8, according to [60]. The tensile strength ranges from $\sigma_{t\beta w} = -3.8$ MPa at $\beta_w = 90°$ to $\sigma_{t\beta w} = -4.6$ MPa at $\beta_w = 0°$.

The regressions carried out with HBm at different β_w were set up by using the complete data set (uniaxial, triaxial and Brazilian tests). The linear regression of the data [σ_3, $(\sigma_1 - \sigma_3)^2$] enabled the calculation of the instantaneous uniaxial compressive strengths $\sigma_{c\beta w}$ and the instantaneous constants $m_{\beta w}$. Table 1 reports the rock properties obtained through this process.

Table 1. Strength parameters of the shale obtained with the HBm regression of lab data.

β_w (°)	$\sigma_{c\beta w}$ (MPa)	$m_{\beta w}$ (-)
0	25.97	3.90
30	20.09	4.69
45	17.40	4.39
60	18.12	5.60
90	29.60	7.16

Figure 6a shows that the calculated uniaxial compressive strength matches well with the results of the lab tests. The figure indicates that the lower uniaxial compressive strength measured in lab tests ($\sigma_{c\beta w} = 15.27$ MPa) occurs at $\beta_w = 60°$. The minimum uniaxial compressive strength obtained from the regression ($\sigma_{c\beta w} = 17.40$ MPa) occurs at $\beta_w = 45°$.

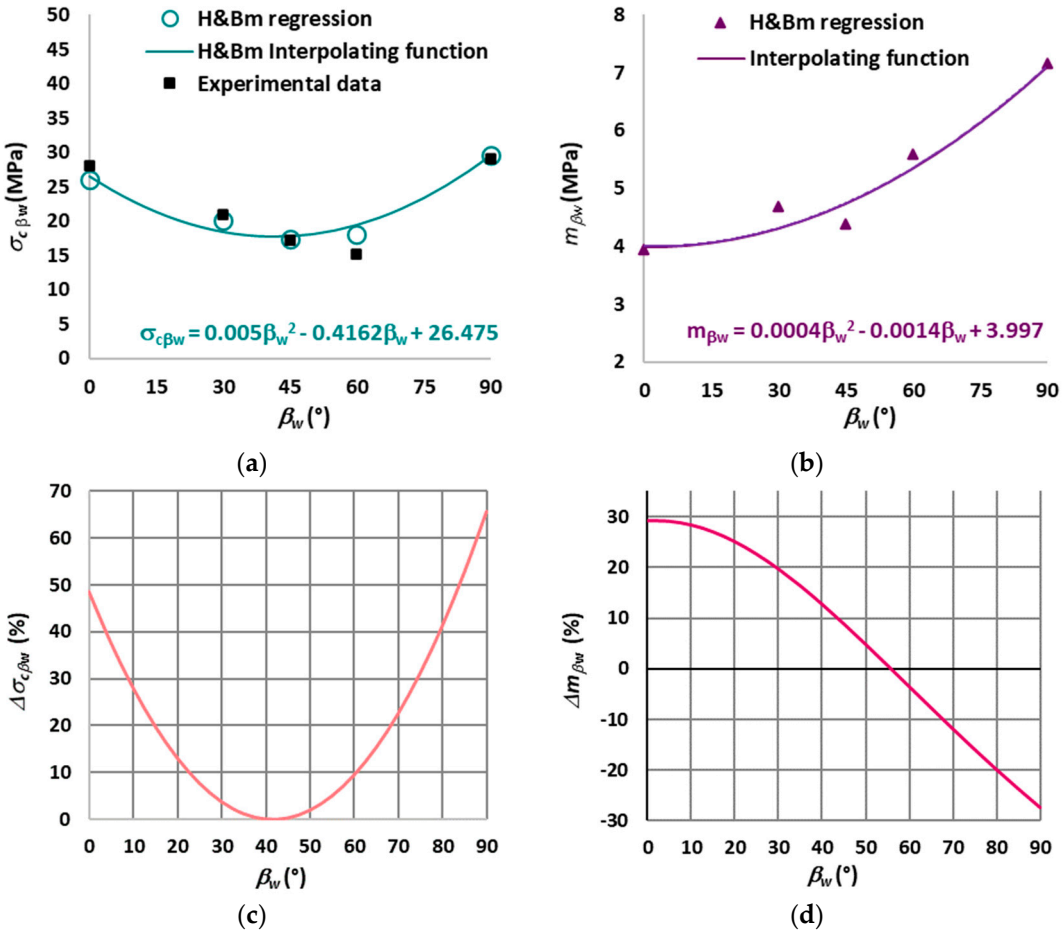

Figure 6. Interpretation of lab data with HBm (**a**) Comparison between the uniaxial compressive strength $\sigma_{c\beta w}$ obtained with the regression (open symbol) and the experimental data of the Tournemire shale (solid symbol). The solid line is the interpolating function. (**b**) Values of $m_{\beta w}$ obtained with the regression and the interpolating function. (**c**) Percentage increase in uniaxial compressive strength $\sigma_{c\beta w}$ from the minimum $\beta_w = 40°$. (**d**) Percentage increase/decrease calculated between $m_{\beta w}$ = 5.16 and the function of $m_{\beta w}$.

Figure 6a also shows the interpolating function of the regression data of $\sigma_{c\beta w}$. The function is a second-order polynomial (parabola), which is used for the calculation of the mud pressure with Equation (6). The minimum of the parabola occurs close to $\beta_w = 40°$. The effect of this mismatch on the mud pressure will be discussed in the next section. Figure 6c shows the percentage increase in uniaxial compressive strength $\sigma_{c\beta w}$ compared to the minimum at $\beta_w = 40°$. The maximum percentage increase occurs at $\beta_w = 90°$ and $\beta_w = 0°$, as expected.

The instantaneous constants $m_{\beta w}$ (Figure 6b and Table 1) change with β_w from $m_{\beta w}$ = 3.90 to $m_{\beta w}$ = 7.16, in agreement with the value of $m = 6 \pm 2$, suggested by [61], for shale. Figure 6b also shows the interpolating function of the regression data of $m_{\beta w}$, which is a second-order polynomial (parabola).

It is worth to note that the instantaneous dimensionless constant $m_{\beta w}$ does not exhibit a well-defined trend in several data regressions [52] and an average value must be assumed. The average value for our dataset is $m_{\beta w}$ = 5.16. Figure 6d shows the percentage increase/decrease calculated with $m_{\beta w}$ = 5.16 and the function of $m_{\beta w}$. The figure indicates that the variation is ≅ ±30% and in the range $\beta_w = 0°–55°$ $m_{\beta w}$ = 5.16 is higher than the $m_{\beta w}$ of the function. We investigated the mud pressure sensitivity to the instantaneous constants $m_{\beta w}$ in Section 4.

Figure 7a shows the comparison between the experimental results and the linear regression data obtained with WPM. The figure shows two regressions that were obtained

with the complete experimental dataset (CD) and with the experimental data set without the Brazilian tests (NB). The figure indicates that the best matching of the experimental data is obtained with the regression without the Brazilian tests. The value of the uniaxial compressive strength at $\beta_w = 0°$ and $\beta_w = 90°$ for the CD regression are quite lower than the measured data. The figure also shows the WPM functions obtained with the two regressions. Both functions do not properly match the experimental data. However, the lowest value of the uniaxial compressive strength which occurs at $\beta_w = 60°$ is equal for both cases and is in agreement with the experimental data. This fact indicates that the cohesion c'_w and the friction angle ϕ'_w of the weakness planes are very close in both cases.

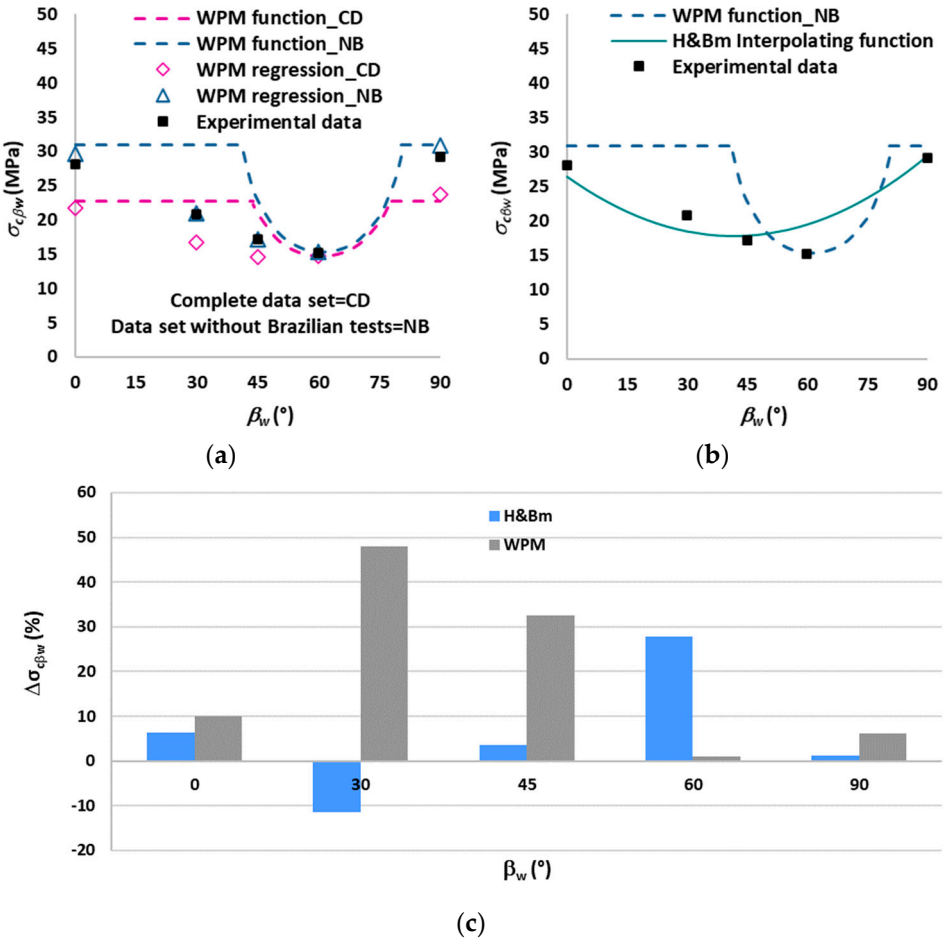

Figure 7. (**a**) Comparison between the uniaxial compressive strength $\sigma_{c\beta w}$ obtained with the WPM regression (open symbol) and the experimental data of the Tournemire shale (solid symbol). The dotted lines are the WPM functions. (**b**) Comparison between the WPM and H&Bm functions and the experimental data. (**c**) Percentage change in $\sigma_{c\beta w}$ calculated with WPM and H&B and the experimental data.

In the end, the strength parameters of WPM were calculated with the NB regression data. The cohesion c'_w and the friction angle ϕ'_w of the weakness planes were calculated at $\beta_w = 60°$ where the lowest value of the uniaxial compressive strength occurs. The plateau strength (c' and ϕ'), which should correspond to the strength of the rock matrix, was calculated at $\beta_w = 90°$, with the M-C criterion. Table 2 reports these parameters. The plot of WPM in the diagram (β_w–$\sigma_{c\beta w}$) was obtained by finding the intersection of the plateau of constant strength with Equation (2a).

Table 2. Strength parameters of the Tournemire shale obtained with the WPM regression of lab data.

	ϕ'_w (°)	c'_w (**MPa**)
Weakness planes	32	4.26
Plateau	33	8.37

Figure 7b shows the comparison between the experimental uniaxial compressive strength $\sigma_{c\beta w}$ and the interpolating function of the HBm and WPM. The figure indicates that the best data matching is obtained with HBm. Figure 6c shows the percentage change in uniaxial compressive strength between the functions and the experimental data. The figure indicates that WPM overestimates $\sigma_{c\beta w}$ for all the inclinations of the weakness planes β_w with a maximum $\Delta\sigma_{c\beta w}$ = +48.06% at β_w = 30°. HBm also overestimates $\sigma_{c\beta w}$ for all the inclinations except at β_w = 30°, with a maximum $\Delta\sigma_{c\beta w}$ = +27.72% at β_w = 60°. The overestimation of the uniaxial compressive strength is undoubtedly higher for WPM.

3.2. *Variation of the Shale Properties with Wellbore Azimuth*

WPM predicts the rock strength with two couples of constant strength parameters: the cohesion and friction angle of the plateau and weakness planes. The parameters remain constant and the variation of the strength is ruled by the change in β_w (Figure 5b).

HBm exhibits a continuous variation of the strength with the two instantaneous parameters, that can be calculated at any wellbore azimuth with the interpolating functions. Figure 8 shows the plots of the trend of $m_{\beta w}$ and $\sigma_{c\beta w}$ at the boundary of the wellbore with different δ. Wellbore azimuths with the lower strength do not necessarily correspond to failure zones. The induced state of stress S and the pore fluid pressure p_f can also influence the location of the failure zones.

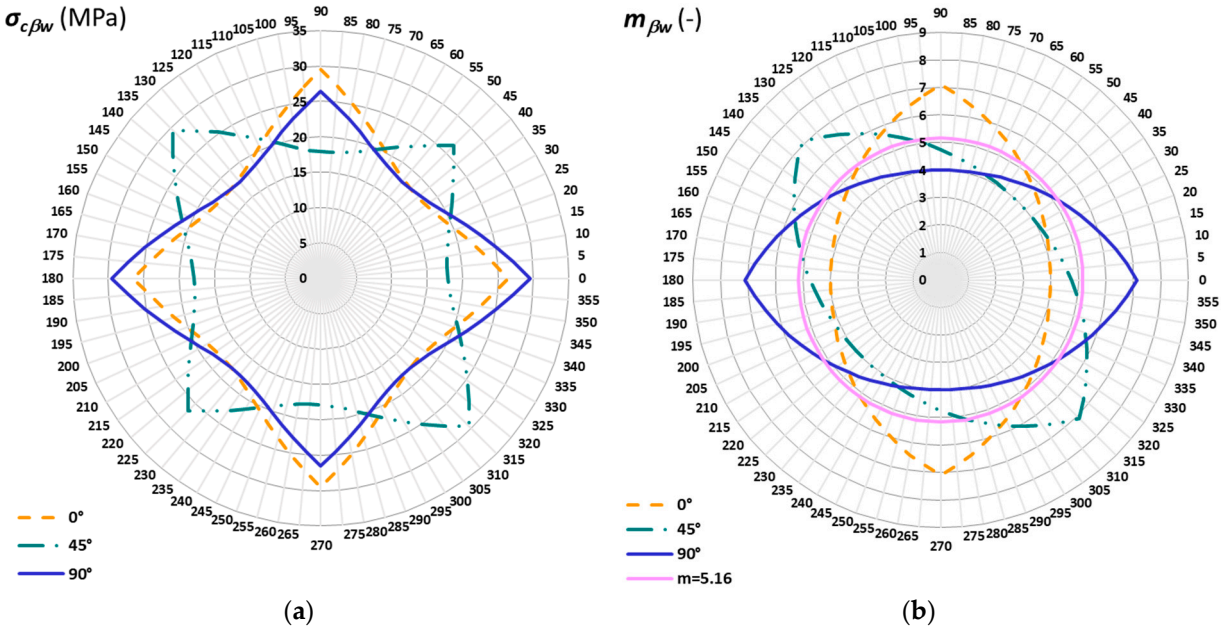

Figure 8. Variation of the parameters of the Tournemire shale with wellbore azimuth ϑ for different δ = 0°–45°–90° (see Figure 4). (**a**) Instantaneous uniaxial compressive strength $\sigma_{c\beta w}$. (**b**) Instantaneous constant $m_{\beta w}$. The pink line corresponds to the average instantaneous dimensionless $m_{\beta w}$ = 5.16.

4. Sensitivity Analyses: Results and Discussion

This section reports the results of the sensitivity analyses of mud pressure predicted by WPM and HBm, by varying the far field stresses and pore fluid pressure and the frictional component of strength. These parameters are often uncertain in real cases. The

sensitivity analyses aim to investigate the responses of the two criteria and highlight the reliability of each model in different field contexts.

4.1. Synthetic Case Studies

We carried out a sensitivity analysis of synthetic cases. We assumed a wellbore drilled in Tournemire shale whose properties are reported in Tables 1 and 2. In the majority of analyses, we assumed that the instantaneous dimensionless constant $m_{\beta w}$ is fixed at the average value $m_{\beta w}$ = 5.16. The effect of the variation in $m_{\beta w}$ with wellbore azimuth on the magnitude of the mud weight is discussed in Section 4.2.

Table 3 reports the assumed far field stresses and pore fluid pressures. Finally, we assumed that the conditions are undrained with $\Delta p_f = 0$, immediately after drilling (see Section 2.2).

Table 3. Far field stresses and pore fluid pressures of synthetic cases.

$R = \sigma_{MAX}/\sigma_{min}$	σ_{MAX} (MPa)	σ_{min} (MPa)	p_f (MPa)
1.0	20	20	11
1.0	33	33	11
1.0	33	33	15
1.1	20	22	0
1.1	20	22	8
1.1	20	22	11
1.25	20	25	8
1.25	20	25	11
1.5	20	30	0
1.5	20	30	11
1.5	20	30	15
1.75	20	35	11
2.0	20	40	11

The geomechanical analysis of borehole stability is carried out by using stresses and pressures and is subsequently converted into mud weight (density units) [46]:

$$\rho_{mud} = \frac{p_w}{gz}, \tag{7}$$

where ρ_{mud} is the mud density, g is gravity and z is the depth.

All the subsequent sensitivity analyses are presented in terms of specific gravity (SG = ρ_{mud}/ρ_{water}), by assuming z = 1000 m, for the comparison of different cases.

4.2. Comparison between Mud Weight Patterns Calculated with WPM and HBm

Figure 9 shows the mud weight (SG) calculated at different inclinations of the weakness plane δ for some of the synthetic cases reported in Table 3. The figure also shows the mud weight of the rock matrix calculated with Equation (5b) for WPM.

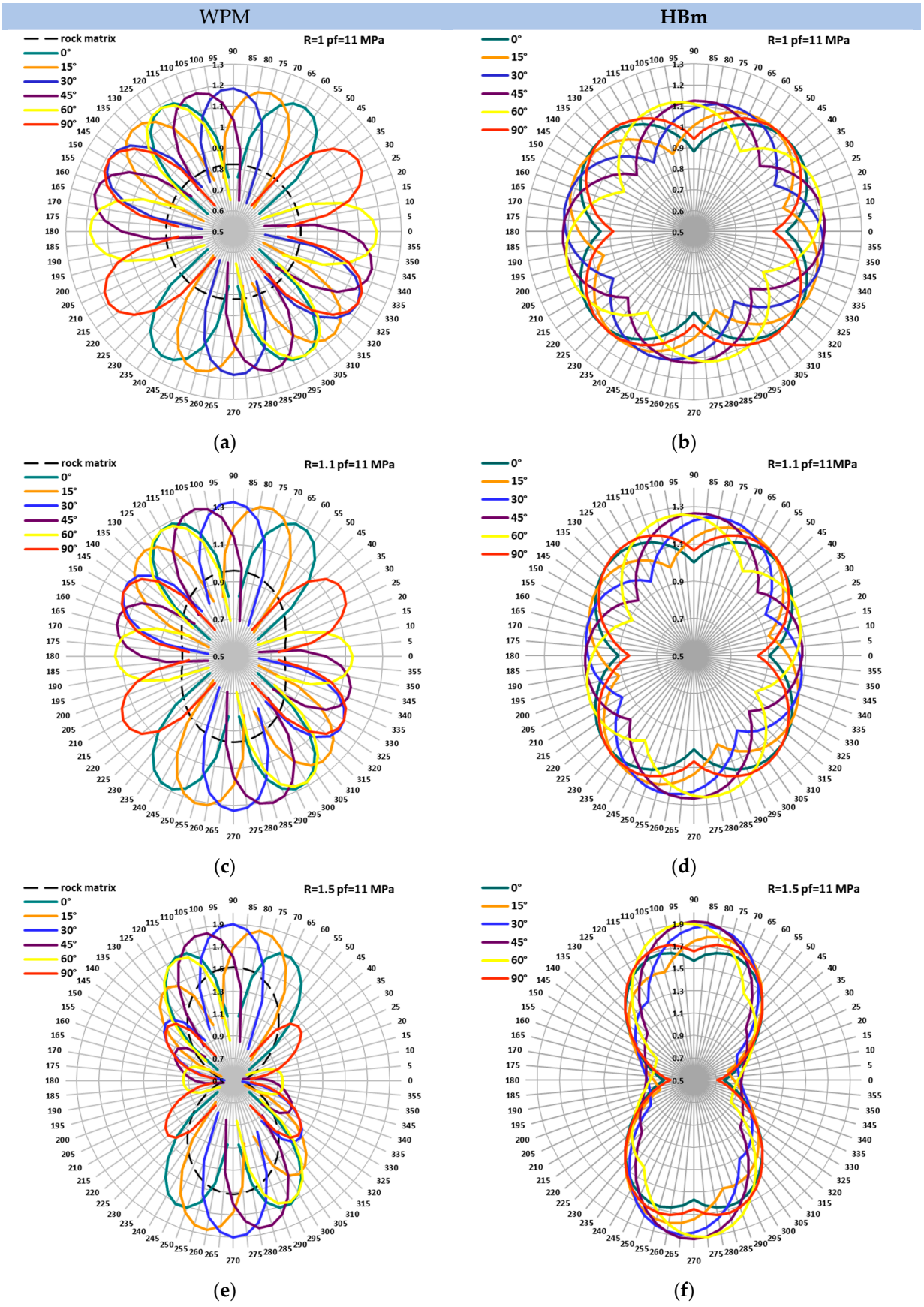
WPM
HBm
rock matrix
0°
15°
30°
45°
60°
90°
R=1 pf=11 MPa
(a)
(b)
R=1.1 pf=11 MPa
R=1.1 pf=11MPa
(c)
(d)
R=1.5 pf=11 MPa
(e)
(f)

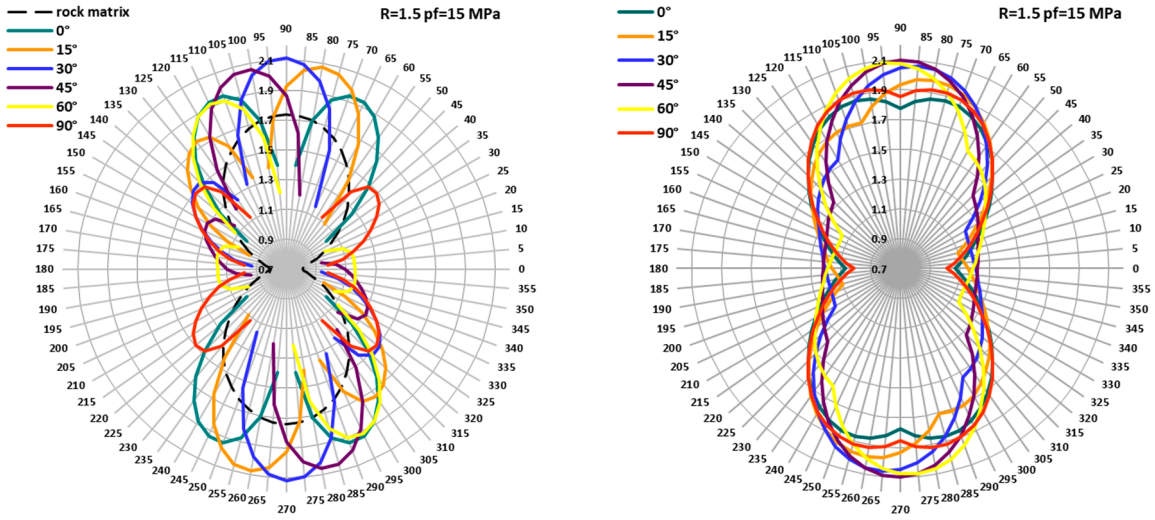

Figure 9. Comparison of SG calculated with WPM (**a**,**c**,**e**,**g**) and HBm (**b**,**d**,**f**,**h**) at different inclinations of the weak planes δ, far field stresses $R = \sigma_{MAX}/\sigma_{min}$ and pore fluid pressures p_f. SG related to the plateau strength is called the rock matrix. The instantaneous dimensionless constant was fixed at the average value $m_{\beta w} = 5.16$.

A rough analysis of these results indicates an agreement of the trends of the mud weight calculated with WPM and HBm.

Figure 9a,b (case $R = 1$) show that the peaks of mud weight occur four times and have the same values for all the inclinations of the weakness plane δ.

Figure 9c–h (cases $R > 1$) show that the far field stress anisotropy influences the number of peaks of the mud pressures. The peaks occur twice, except for $\delta = 0°$ and $\delta = 90°$. Figure 9 shows that the positions of the peaks calculated with the two criteria at a given δ have different azimuths. The magnitude of the mud weight peaks is generally different in the two predictions.

Figure 9e–h (cases $R = 1.5$) show an elongated pattern of the mud pressures towards $\vartheta = 90°$ for both criteria, because of the high far field stress anisotropy.

4.3. *Influence of the Far Field Stresses and Pore Fluid Pressure on Mud Weight Prediction*

The results reported in Section 4.2 evidenced some influence of the far field stresses and pore fluid pressure on the mud weight calculated with WPM and HBm. We investigated this influence with comparative analyses.

Figures 10 shows a quantitative comparison of SG shown in Figure 9 and Table 3. The figure shows that almost all mud weights with $R > 1$ are well approximated with second-order polynomial functions (solid and dotted lines).

Figure 10a (case $R = 1$) shows that SG calculated with WPM is slightly higher than the SG calculated with HBm, when the far field stresses are 20–20 MPa with $p_f = 11$ MPa and 33–33 MPa with $p_f = 15$ MPa. On the other hand, SG coincide when the far field stresses are 33–33 MPa with $p_f = 11$ MPa. The reason for the mismatch and coincidence of the two approaches can be attributed to the different sensitivity to the far field stresses and pore fluid pressure.

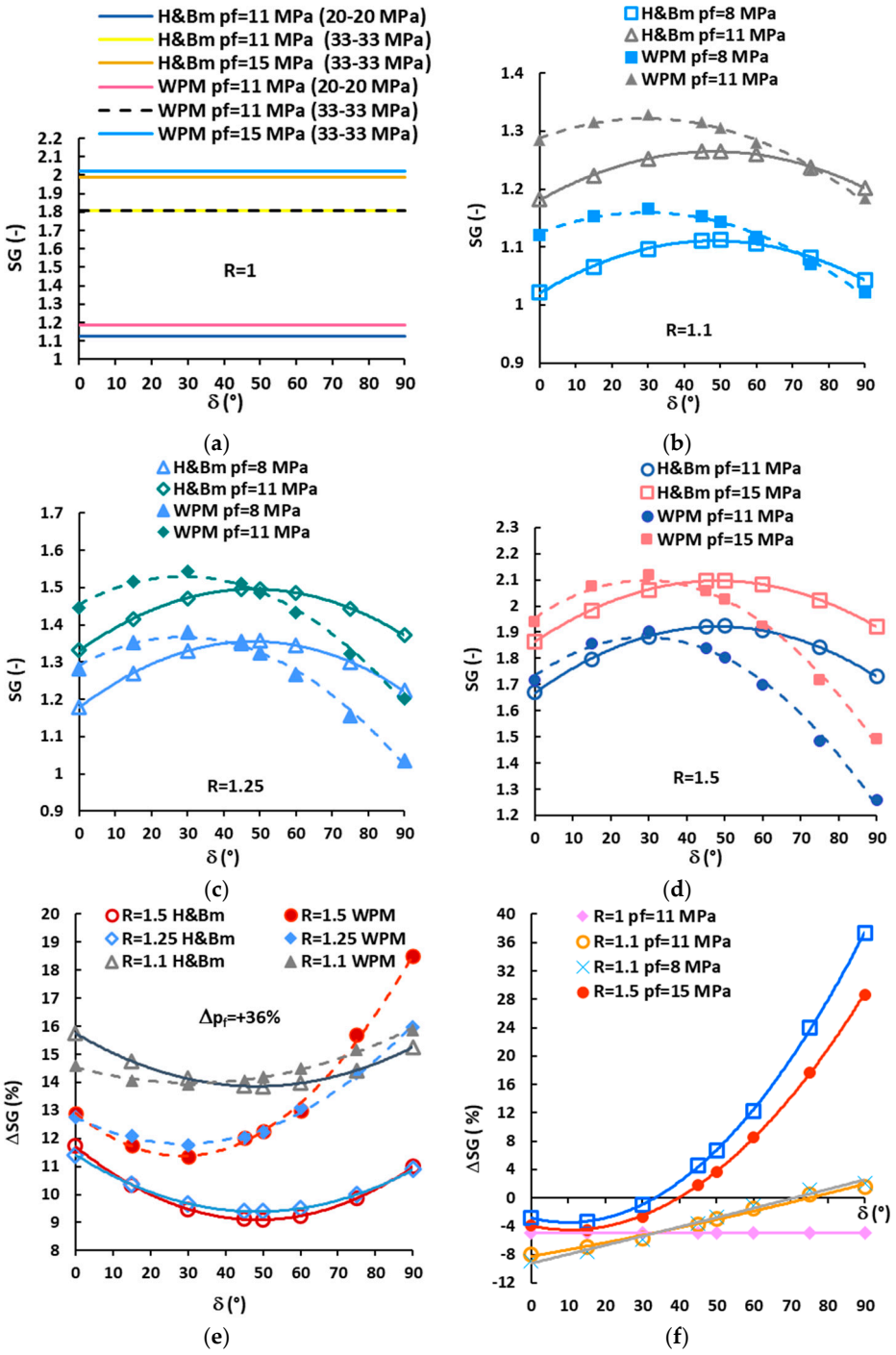

Figure 10. (**a**) Quantitative comparison between SG calculated with WPM and HBm. (**a**) $R = 1$ and p_f = 11–15 MPa. (**b**) $R = 1.1$ and p_f = 8–11 MPa. (**c**) $R = 1.25$ and p_f = 8–11 MPa. (**d**) $R = 1.5$ and p_f = 11–15 MPa. (**e**) Variation percentage of SG calculated with WPM and HBm with variation of the pore fluid pressure from p_f = 11 MPa to p_f = 15 MPa, resulting in a percentage increase in Δp_f = +36%. (**f**) Percentage change in SG calculated with HBm and WPM.

In all cases with $R > 1$, the SG calculated with the two criteria are alternatively higher/lower as a function of the inclination δ and the far field stress anisotropy R (Figure 9b–d). The trend for mud weight with δ is practically parallel in each approach. WPM predicts higher SG in the range $\delta = 0°–45°$ and lower SG in the range $\delta = 45°–90°$ at high R.

Figure 10b–d indicate that the difference between WPM and HBm predictions does not change with the magnitude of the pore fluid pressure. In fact, the change in trend

(higher/lower SG) almost always occurs at the same δ, regardless of the variation of the pore fluid pressure.

The increase in pore fluid pressure (see Table 3) is Δp_f = +36% (case R = 1.5) and Δp_f = +37% (cases R = 1.1 and R = 1.25). This increase is practically equal. Figure 10e shows the percentage change in SG with the change in pore fluid pressure Δp_f. The figure indicates that the percentage increase in SG is higher at R = 1.1 for both criteria. This result indicates that SG is more sensitive to an increase in pore fluid pressure at low anisotropy of the far field stresses. The maximum SG always occurs at δ = 0° (HBm) and at δ = 90° (WPM). The difference between the percentage change in SG calculated with the two criteria becomes relevant when R > 1.1 and δ > 50°. The trends of the percentage change obtained with HBm are almost parallel for all cases (R = 1.1, R = 1.25 and R = 1.5). On the other hand, the trends of the percentage change obtained with WPM vary with R, with a remarkable rise from δ = 30°to 90°, when R = 1.5.

Figure 10f shows the comparison between the WPM and HBm predictions of SG, in terms of percentage change, when R = 1.1 and R = 1.5. The figure shows that the most significant decrease in SG of HBm (−9%), occurs when R = 1.1 at δ = 0°. The range δ = 75°–90° exhibits a lightly higher SG calculated with HBm (+2%).

On the other hand, the percentage decrease in HBm reduces when R = 1.5. In this case, the percentage increase in HBm is very high (+29–40%) from δ = 40° to δ = 90°. The reason for this high mismatch appears to be the remarkable decrease in WPM mud weight when R > 1.1 (Figure 10c,d). Finally, the figure shows that the change in trend (higher/lower SG) predicted by WPM and HBm is independent of the pore fluid pressure magnitude.

We performed a quantitative comparison between the predictions of WPM and HBm, by varying the far field stress anisotropy. Figure 11a,b show the comparison of the mud weight predicted by the two criteria at different R with constant pore fluid pressure. The figures indicate that the change in trend (higher/lower SG) occurs when R > 1.1. Furthermore, HBm predicts a definitely higher mud weight when R > 1.5 for all the inclinations δ of the weak planes. This outcome indicates that WPM provides questionable mud weights at high R, in the range δ = 50°–90°.

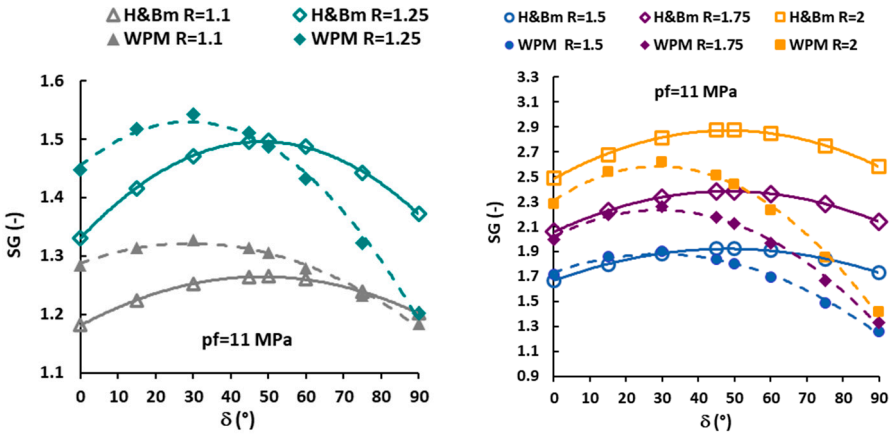

(**a**) (**b**)

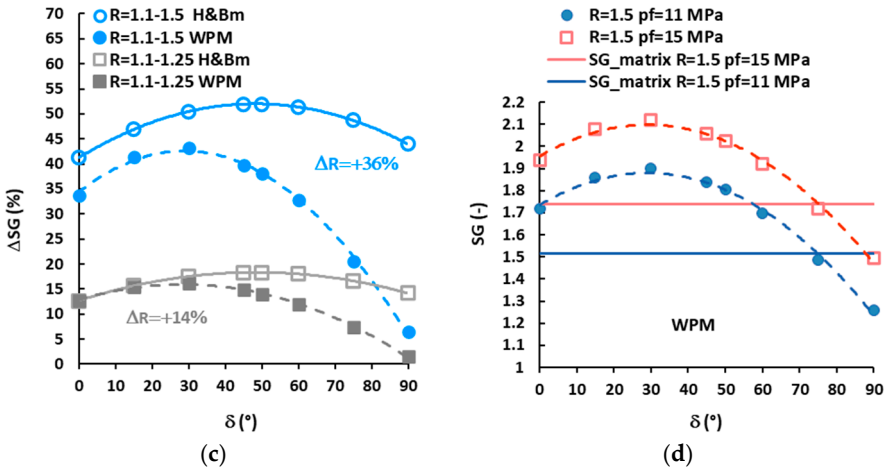

Figure 11. (**a**) Comparison between the mud weight trends at different R = 1.1–1.25 and constant pore fluid pressure p_f = 11 MPa. (**b**) Comparison between the mud weight trends at different R = 1.5–2.0 and constant pore fluid pressure p_f = 11 MPa. (**c**) Percentage change in SG related to percentage change in far field stresses ΔR = +36% and ΔR = +14% at constant pore fluid pressure p_f = 11 MPa. (**d**) Comparison between SG of the weakness planes and rock matrix (plateau of constant strength) when R = 1.5 and p_f = 11–15 MPa.

Figure 11c shows the percentage change in SG with the variation of the far field stresses ΔR (at constant pore fluid pressure p_f = 11 MPa). The change in R from 1.1 to 1.5 corresponds to ΔR = +36% and the change in R from 1.1 to 1.25 corresponds to ΔR = +14%. The figure indicates that the variation of SG calculated with HBm is more sensitive to the increase in far field stress anisotropy, especially from δ = 30° to δ = 90°. The change in SG calculated with HBm is overall higher, except for a few inclinations of the weakness planes with ΔR = +14%, and shows a maximum at δ = 45°. On the other hand, the change in SG calculated with WPM after the peak exhibits a substantial decrease from δ = 30° to δ = 90°. This prediction seems to be anomalous, particularly close to δ = 90°.

Figure 11d shows the comparison between the SG of the weakness planes and rock matrix when R = 1.5. In general, the SG of the rock matrix is expected to be lower than the SG of the weak planes. Nevertheless, the figure clearly shows that the SG of the rock matrix is higher than the SG of the weakness planes in the range δ = 75°–90°. On the other hand, the peaks calculated with HBm (Figure 11a–c) are higher than the peaks of the rock matrix in the range δ = 45°–90°.

The change in trend (higher/lower SG) of the predictions with WPM and HBm occurs with increasing R. This change depends on the interpolating functions of the strength. WPM provides anomalous results when R > 1.1. These outcomes are related to the constrain of the minimum strength at $\beta_w = 45° + \phi'_w/2$ and the fast growth of the interpolating function.

Figures 10 and 11 indicate that the maximum mud weight occurs at a specific inclination $\delta = \delta_{crit}$ of the weakness planes, irrespective of R and p_f. The maximum SG predicted by WPM always occurs at $\delta_{crit} = 45° - \phi'_w/2$, as found by [52] and in this paper (δ_{crit} = 30°). On the other hand, the maximum SG predicted by HBm occurs at δ_{crit} = 50° with β_w = 40°, which corresponds to the minimum strength of the interpolating function.

The analysis of the location of the mud weight peaks at different δ evidenced that the correspondent angles β_w have different distribution. Figure 12 shows the frequency distribution of the angles β_w at which the peaks of the mud weight occur. The distribution of the angles β_w was calculated at different far field stresses (R = 1–1.5), pore fluid pressures (8 MPa, 11 MPa and 15 MPa) and inclination of the weakness planes (δ = 0°–15°–30°–45°–50°–60°–90°).

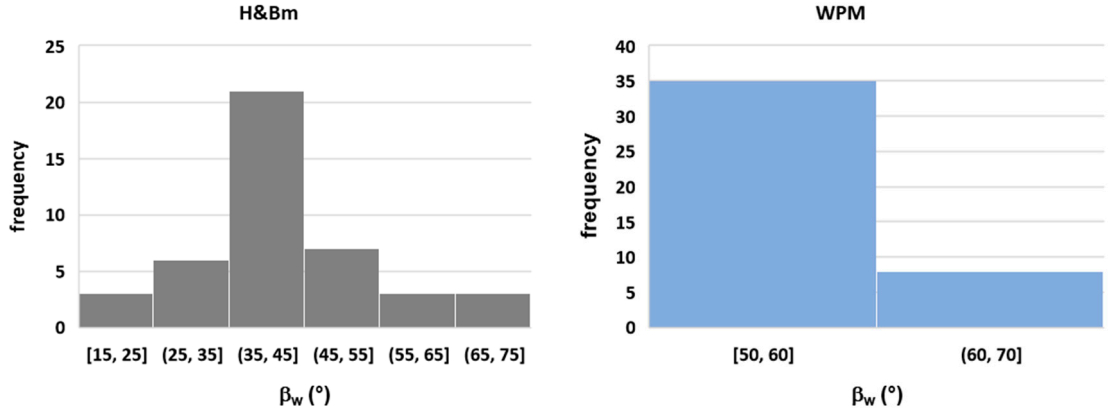

Figure 12. Frequency distribution of the angles β_w at which the mud weight peaks occur by varying the weakness plane inclination δ, far field stresses $R = \sigma_{MAX}/\sigma_{min}$ and pore fluid pressures p_f.

The peaks calculated with HBm occur in a wide range of β_w = 15°–75°. The range of β_w is affected by the far field stress anisotropy R. Furthermore, the pore fluid pressure magnitude does not seem to influence the location of the peaks, although the high variation Δp_f = +37%.

The peaks calculated with WPM occur in the range β_w = 50°–70°. Most peaks occur at β_w = 60°, which corresponds to the minimum strength $\beta_w = 45° + \phi'_w/2$. This result suggests that the mud weight is lightly influenced by the anisotropy of the far field stresses R and heavily depends on the minimum strength. Furthermore, the pore fluid pressure magnitude negligibly affects the location of peaks.

These outcomes can explain why SG calculated with WPM are higher/lower than the peaks calculated with HBm. Finally, HBm is more sensitive to the far field stress anisotropy than WPM, in terms of β_w.

4.4. Influence of the Frictional Component of Strength on the Mud Weight Prediction

We investigated the mud pressure sensitivity to the frictional component of strength. We increased the friction angle of the weakness planes from ϕ'_w = 32° (Table 2) to ϕ'_w = 38°. The percentage increase is $\Delta\phi'_w$ = +19%. Figure 13a shows the percentage decrease in SG at different R and pore fluid pressures p_f. The figure indicates that the maximum change occurs close to δ = 50°–60° for all cases. The minimum change occurs at δ = 0°. The maximum SG change occurs when R = 1.5 and p_f = 11 MPa. The SG change increases with R and is mitigated by high pore fluid pressure.

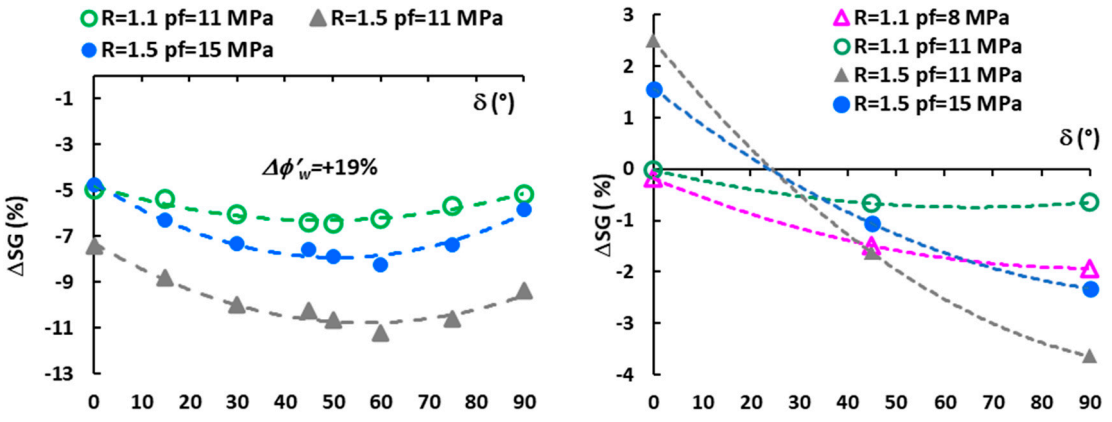

Figure 13. (**a**) Percentage decrease in SG related to the increase in friction angle of the weakness planes from ϕ'_w = 32° to ϕ'_w = 38° at different R and p_f. (**b**) Percentage increase/decrease in SG calculated with $m_{\beta w}$ =5.16 and the function of $m_{\beta w}$.

The instantaneous dimensionless constant $m_{\beta w}$ of HBm can be considered as a frictional component of the rock strength [62]. Figure 6d shows the percentage increase/decrease in frictional strength calculated with $m_{\beta w}$ = 5.16 and the function of $m_{\beta w}$. The figure indicates that the variation is ≅ ±30%. The constant $m_{\beta w}$ = 5.16 is higher than $m_{\beta w}$ of the function, in the range β_w = 0°–55°. Figure 13b shows the correspondent change in SG and indicates that SG is lightly underestimated with the average value $m_{\beta w}$ = 5.16, when R = 1.1, with a maximum decrease of −1.9%. Furthermore, an overestimation of SG (+2.5%) with the average value $m_{\beta w}$ = 5.16 occurs in the range of inclinations δ = 0°–30° when R = 1.5. The underestimation of SG occurs in the range δ = 25°–90°. The more remarkable underestimations occur at δ = 90°, in all cases. The more substantial underestimation of SG occurs at high far field stress anisotropy, but an increase in pore fluid pressure reduces the magnitude of the underestimation. This outcome indicates a mitigation effect of the pore fluid pressure on the overestimation of the frictional strength, as found with WPM. The previous discussion indicates that the change in frictional strength component lightly influences the peak of mud pressure. In fact, the influence of a high change in frictional strength produces a small underestimation of the mud weight (−3.6%), in the worst case ($\Delta m_{\beta w}$ = +27%). The mud weight calculated with WPM results in being more sensitive to the change in frictional strength.

Finally, the assumed constant value $m_{\beta w}$ = 5.16 is in agreement with m = 6 ± 2 suggested by [61] for shale, and the majority of $m_{\beta w}$ calculated from lab tests by [52–54].

4.5. Comparison of the Results with Other Studies

There is a wide literature on wellbore stability in shales. The influence of thermo/hydro/mechanical coupling and multi-planes on mud pressure prediction is generally carried out with WPM (i.e., [14,36,63–67]). The majority of studies reports predictions of mud weight carried out with WPM in synthetic cases or real cases by systematically varying wellbore azimuth and inclination. Generally, the friction angle and the cohesion of the weakness planes are directly estimated/assumed and not measured in lab.

The reliability of the SG prediction with measured rock properties with WPM is not specifically and quantitatively investigated in other studies. Furthermore, to our knowledge, the prediction of the mud pressure with HBm is just reported in [52–54] and in [68]. The results of our study are in agreement with the results reported in [52–54]. The study reported in [68] analyzes a synthetic case with assumed rock properties and a very low frictional component of strength, that makes the comparison difficult.

These observations highlight the need for further studies related to the analysis of the reliability of mud pressure predictions, based on strength properties of shale from laboratory measurements.

5. Numerical Modeling of Wellbore Stability with WPM and HBm

We carried out numerical simulations of wellbore stability with the code FLAC (Fast Lagrangian Analysis of Continua, ver 8.10, Itasca). FLAC is a two-dimensional explicit finite difference program for engineering mechanic computations.

The computational domain is a radial grid (Fish DONUT, implemented in FLAC) with 60 zones in the radial direction and 60 zones on the circumference. The wellbore diameter is 1 m and the diameter of the grid is 40 m (Figure 14). The state of stress within the model is initialized by imposing σ_{MAX} in the horizontal and σ_{min} in the vertical direction. The same horizontal and vertical stresses are applied at the external boundary of the grid. The grid is configured for fluid flow analysis. The undrained conditions used in the analytical solution (constant pore fluid pressure Δp_f = 0) are obtained by (a) imposing and

fixing the pore fluid pressure (p_f); (b) imposing the bulk modulus of the fluid equal to zero; (c) setting of the mechanical calculations and turning off the fluid flow calculations.

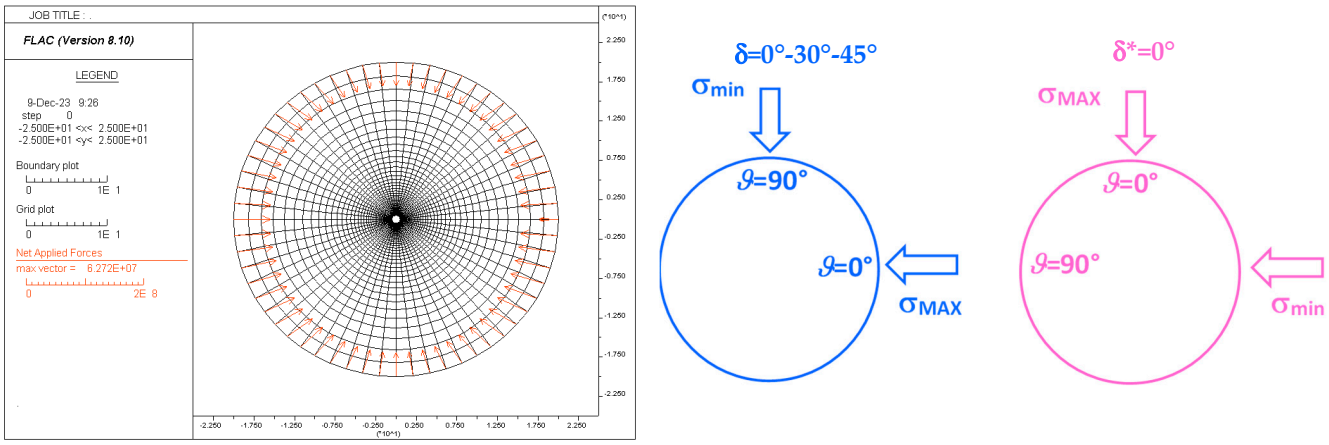

(**a**) (**b**)

Figure 14. (**a**) Grid used in the numerical simulations with FLAC. Notation: *10^1 = ×10[1] m (**b**) Directions of the far field stresses used in the simulations.

A mechanical pressure, equal to the mud pressure calculated with the analytical solution, is applied at the internal boundary (wall of the borehole). A higher mechanical pressure avoids slip or failure in the rock matrix. A lower mechanical pressure results in an enlargement of the failed zone and possibly in borehole collapse.

We carried out numerical simulations with the Ubiquitous Joint Model (UBI) and HB criterion for isotropic rock. Both constitutive laws are a continuum based model.

UBI accounts for joint implicitly: the weakness planes are smeared across the rock mass (ubiquitous) with a given inclination (δ). At first the code detects general failure with the M-C in the rock matrix and applies plastic corrections. The corrected stresses are then analyzed for failure on the weakness plane with the WPM, and updated accordingly.

Figure 15 shows the results of the numerical simulations carried out with $R = 1.5$ with $p_f = 11$ MPa at $\delta = 0°$–$30°$–$45°$–$90°$ carried out with UBI. The pattern of failure location at $\delta = 0°$, $\delta = 30°$ and $\delta = 45°$ shown in Figure 15a–c is in agreement with the peaks shown in Figure 9e. Figure 15d shows the results of the numerical simulations carried out at $\delta^* = 0°$, with the new reference system (see Figure 5c). The figure clearly shows that there is the occurrence of plasticity in the rock matrix (at $\vartheta = 90°$) and, surprisingly, slip does not occur along the weakness planes, in agreement with the anomalous predictions shown in Figures 9e and 11d. The agreement between the results obtained with the WPM and UBI does not indicate that the prediction of the mud pressure at $\delta^* = 0°$ is reliable. Instead, the results indicate that WPM under some field conditions cannot correctly predict mud pressures.

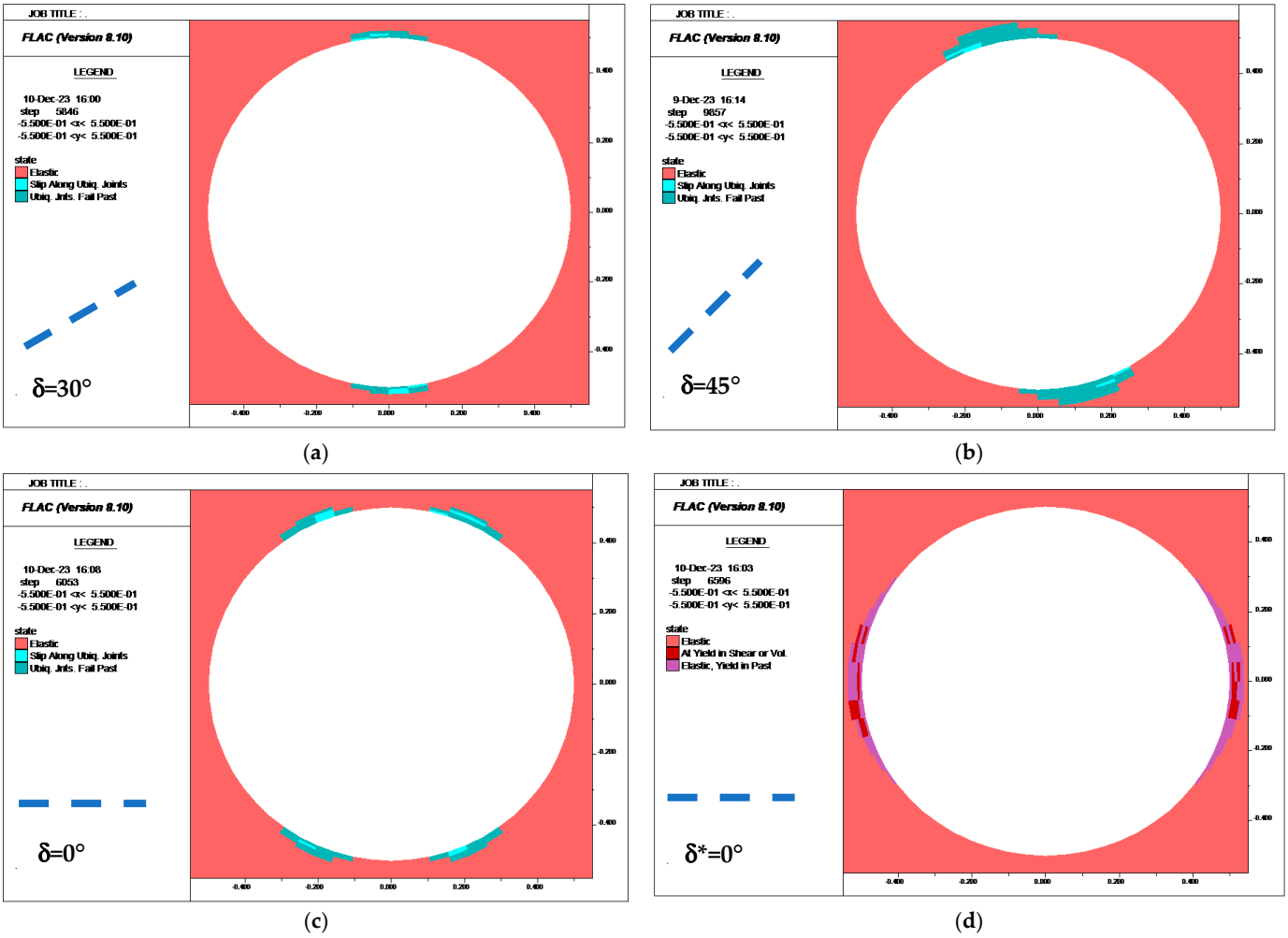

Figure 15. Numerical simulations of slip failure and rock matrix plasticity with UBI. R = 1.5 and p_f = 11 MPa. Legend of colors: light red indicates the elastic state; light cyan indicates slip along the ubiquitous joints at the convergence of the numerical runs; cyan indicates "at yield in past in the weakness planes", i.e., during the numerical convergence; red indicates plasticity in the rock matrix; purple indicates "at yield in past in rock matrix" i.e., during the numerical convergence. The dotted blue line indicates the inclination of the weakness planes. (**a**) $\delta = 30°$. (**b**) $\delta = 45°$. (**c**) $\delta = 0°$. (**d**) $\delta^* = 0°$.

Numerical simulations with HBm, by using the HB isotropic model implemented in FLAC, can be obtained by programming a routine or simply dividing the area around the well into slices with different $\sigma_{c\beta w}$.

The trend of $\sigma_{c\beta w}$ with wellbore azimuth ϑ are shown in Figure 8a. We identified the slices with constant averaged $\sigma_{c\beta w}$ according to Figure 8a. Figure 16a,b show the variation of $\sigma_{c\beta w}$ for the inclination $\delta = 45°$, $\delta = 0°$ and $\delta^* = 0°$.

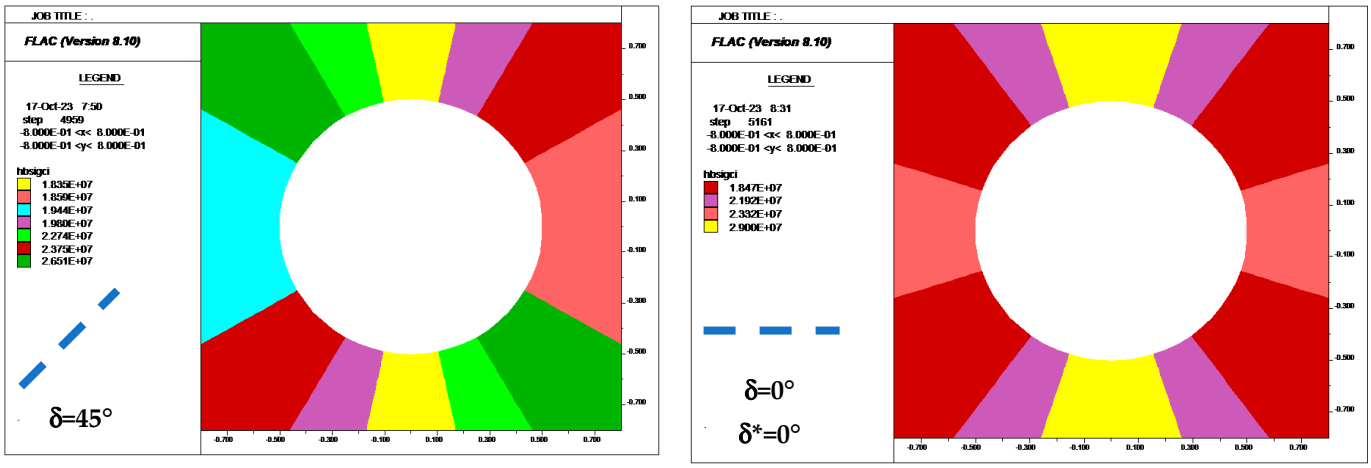

(**a**) (**b**)

Figure 16. Variation of the uniaxial compressive strength $\sigma_{c\beta w}$ used in the numerical simulations with HB criterion. The unit is (Pa). The dotted blue line indicates the inclination of the weakness planes (**a**) $\delta = 45°$. (**b**) $\delta = 0°$ and $\delta^* = 0°$.

The results of the numerical simulations with $R = 1.5$ with $p_f = 11$ MPa are shown in Figure 17. The numerical results shown in Figure 17a–b are in agreement with the analytical predictions. Furthermore, the cases with $\delta = 0°$ and $\delta^* = 0°$ also show plasticity close to $\vartheta = 90°$ (Figure 17c,d). This result is in agreement with Figure 9f, where a very small drop of mud pressure occurs between the peaks. Finally, Figure 17d shows the results of the numerical run carried out with the low mud pressure predicted by the WPM (Figures 9e and 11d). The figure shows a wide plasticity area, indicating that the WPM prediction underestimates the mud pressure of the weakness planes.

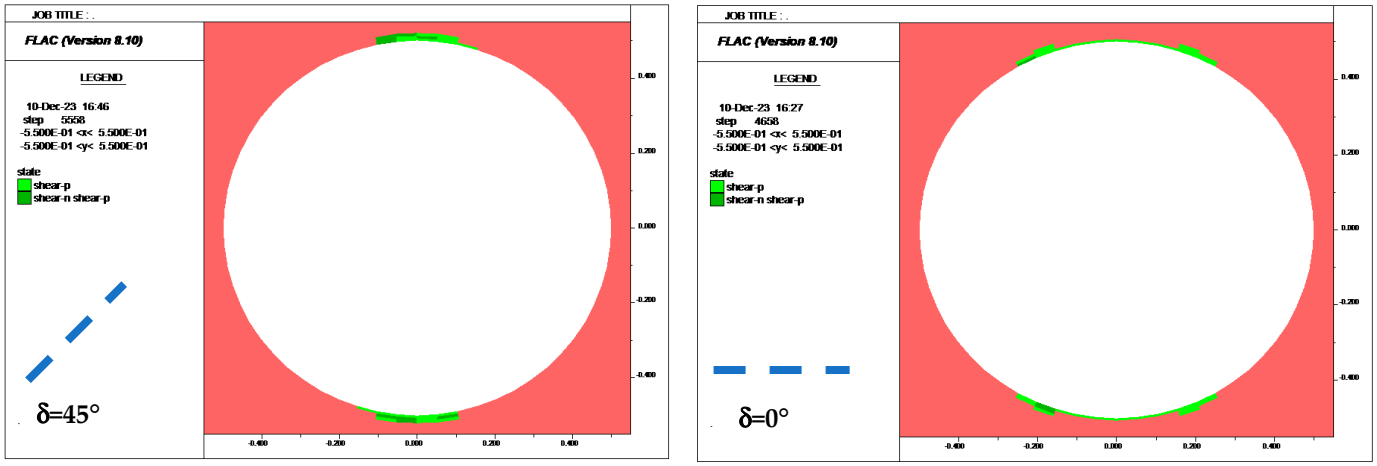

(**a**) (**b**)

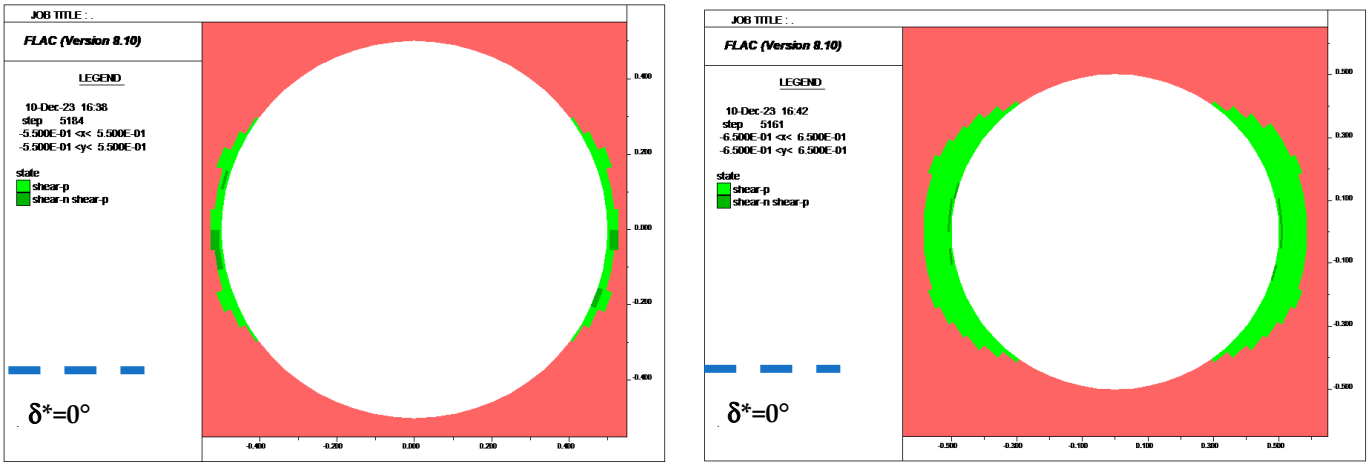

(**c**) (**d**)

Figure 17. Numerical simulations of rock plasticity with HB by using the $\sigma_{c\beta w}$ shown in Figure 16. R = 1.5 with p_f = 11 MPa. Legend of colors: light red indicates the elastic state; dark green indicates at yield; light green "at yield in past", i.e., during the numerical convergence. The dotted blue line indicates the inclination of the weakness planes. (**a**) δ = 45°, (**b**) δ = 0°, (**c**) δ^* = 0°, (**d**) δ^* = 0° calculated with the mud pressure predicted by the WPM (Figure 15e).

The results of all numerical simulations are in agreement with the analytical solutions: the mechanical pressure that induces slip or rock matrix failure is almost equal to the mud pressure calculated analytically. The numerical results obtained with UBI and HB criterion confirm the results obtained with the analytical solutions, also for the anomalous cases. The task is now to identify a reasonable solution for a safe, reliable and simple analysis for the stability of wellbores drilled in anisotropic shale. In the next section, the pros and cons of the WPM and HBm are discussed.

6. Pros and Cons of the WPM and HBm: Conclusions

The results presented in Sections 4 and 5 evidenced that the SG predicted by the HBm is lower than SG predicted by the WPM at least in the range δ = 0°–40°. The highest gap is −9% and occurs when the far field stress anisotropy is R = 1.1. On the other hand, the SG predicted by the WPM is substantially lower than SG predicted by the HBm in the range δ = 40°–90°, when R > 1.1. Furthermore, SG calculated with WPM has a sudden drop, in the range δ = 50°–90°, which appears anomalous. The highest gap is −37% and occurs at δ = 90°when the far field stress anisotropy is R = 1.5. The inclination δ = 90° seems uncommon, as discussed in Section 2.2. However, this case becomes δ^* = 0° (rotated reference system) and can often occur in real fields.

We calculated the coefficient of variation of SG [CV = (Standard Deviation/Mean) × 100]. Figure 18 shows the comparison between the coefficient of variation of SG calculated with the two criteria.

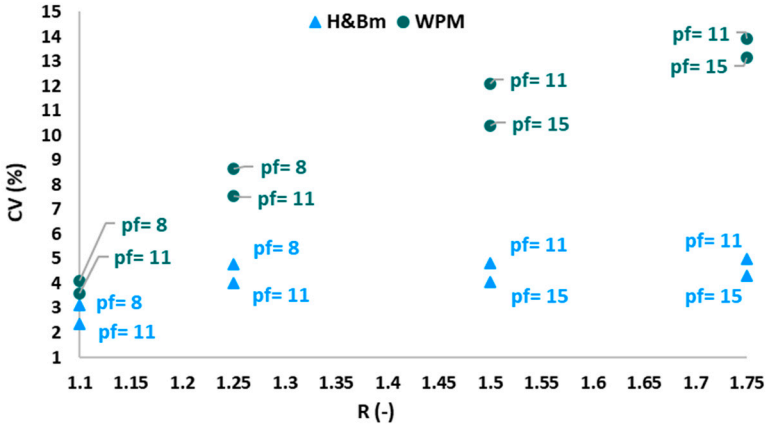

Figure 18. Coefficient of variation of SG at different R and p_f.

The coefficient of variation related to HBm is CV ≤ 3% when R = 1.1 and CV ≤ 5% at higher values of R. The coefficient of variation related to WPM is CV ≤ 4% when R = 1.1 and shows an increasing extent of variability with R. This result confirms that the SG prediction with WPM should be avoided in the range δ = 60°–90° when R > 1.1.

This analysis suggests that a conservative estimate of SG can be obtained with WPM at low far field stress anisotropy and with HBm at high far field stress anisotropy. This conclusion needs further investigations, always based on lab measurements of shale properties. In fact, the HBm function fitted the experimental data of the Tournemire shale quite well, even though the minimum strength is predicted at β_w = 40° and the experimental one is at β_w = 60°. On the other hand, the WPM function fitted the experimental data rather poorly, even though the predicted and experimental minimum strengths occur at the same β_w = 60°.

Figure 12 indicates how many inclinations of the weakness planes must be tested in uniaxial/triaxial compression with the two criteria. The WPM predicts the majority of mud pressure peaks in correspondence of β_w = 50°–60° and therefore needs a lower number of lab tests compared to HBm. Nevertheless, WPM provides anomalous results in some conditions. On the other hand, the WPM is implemented in the majority of the commercial software of geomechanics.

The prediction of SG with WPM and HBm, in a real field, must also take into account the uncertainties in the estimation of the variables that affect the mud pressure: inclination of the weak planes; magnitude of the far field stresses and pore fluid pressure. All these issues suggest that the limit mud weight could be higher than that predicted at a specific δ.

The higher value of SG, which corresponds to δ_{crit}, could be considered the reference SG at least with small δ and low R for HBm and with large δ and high R for WPM. The results of the analyses reported in Section 4 indicated that δ_{crit} = 30° for WPM and δ_{crit} = 60° for HBm.

Figure 19 shows the percentage change in SG between the value calculated at δ_{crit} and the other δ. The percentage change has the highest values at δ = 0° when SG is calculated with HBm and at δ = 90° (which corresponds to δ^* = 0°) when SG is calculated with WPM.

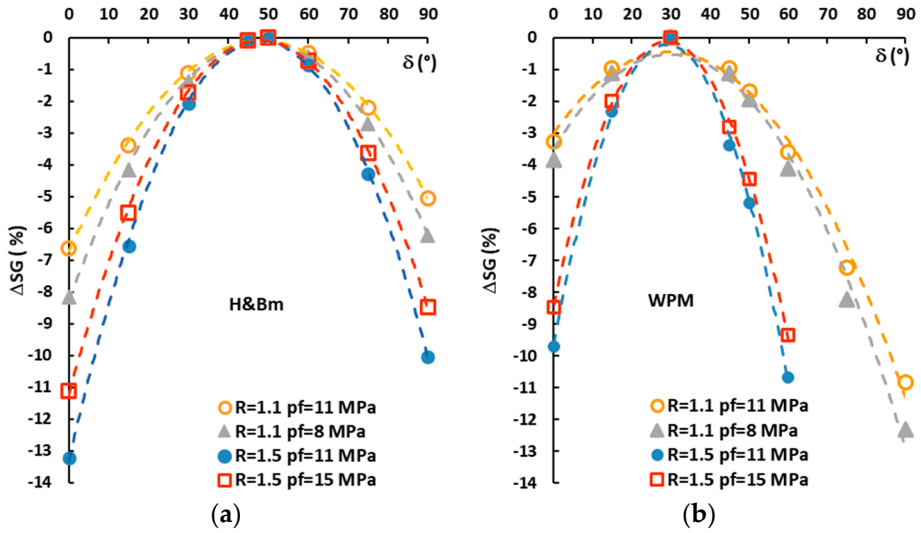

Figure 19. Variation percentage of the mud weight ΔSG between the SG calculated at δ_{crit} and the other δ. (**a**) variation calculated with the HBm. (**b**) variation calculated with the WPM.

As the prediction with HBm seems to "underestimate" (compared to WPM) the mud weight at low R, the use of SG which corresponds to δ_{crit} for R = 1.1 results in a maximum percentage decrease equal to −8% that occurs at δ = 0°. In the range δ = 15°–75°, the maximum percentage decrease is −4% (Figure 19a) The percentage decrease at high R when δ = 0° becomes high (−13%) and the occurrence of tensile failure (hydraulic fracturing) must be carefully investigated in order to find a properly safe mud weight window. According to [52], the lower SG for hydraulic fracturing occurs at δ = 0°.

The maximum percentage decrease calculated with the WPM in the range δ = 15°–45° is −4% for all the far field stress anisotropy R and pore fluid pressures p_f. We highlight that the percentage change in Figure 19b has been truncated at δ = 50° when R = 1.5, because of the anomalous drop that was discussed previously.

Based on the outcomes of this paper and those reported in [52–54], the critical inclination for shales is expected to occur in the range δ_{crit} = 30°–60°. This range of δ_{crit} corresponds to β_w = 40°–60° at the boundary of the borehole. Consequently, the use of δ_{crit}, for the prediction of the mud pressure in cases with other inclinations δ, results in a reduction of the number of compression tests to be carried out for determining the strength parameters, especially with the HBm criterion. The shale specimens can be tested with compression tests at three inclinations within the range β_w = 40°–60°. Finally, the use of the HBm, with the assumption of the dimensional constant fixed at $m_{\beta w}$ = 6 ± 2 for shale rock [61], and the direct use of the uniaxial compressive strength $\sigma_{c\beta w}$ measured (and not obtained from the data regression) with uniaxial compressive tests can avoid carrying out triaxial compressive tests which are costly and challenging.

Future research developments will focus on the same sensitivity analyses of this study coupled with the interpretation of lab tests carried out on shale rocks with WPM and HBm. A further development will be the analysis of a real case of wellbore instability, by using reference mud weights based on the post-drilling experience coupled with the strength properties of shale rock obtained by lab tests.

Author Contributions: Conceptualization, C.D. methodology, C.D.; software, W.L.; formal analysis, C.D.; investigation, C.D. and W.L.; resources, C.D., W.L. and K.Y.; writing—original draft preparation, C.D.; writing—review and editing, C.D., W.L. and K.Y.; supervision, C.D. All authors have read and agreed to the published version of the manuscript.

Funding: Wenjie Liu's scholarship as a visiting PhD student at Politecnico di Torino (PoliTo-CSC) was granted by "Nationally-sponsored Graduate Program of China for High-level Universities". Grant number: (202208340046).

Institutional Review Board Statement: Not applicable.

Informed Consent Statement: Not applicable.

Data Availability Statement: The data presented in this study are available on request from the corresponding author. The data are not publicly available due to privacy.

Conflicts of Interest: The authors declare no conflicts of interest.

Nomenclature

c'_w	Cohesion of the weakness planes
$m_{\beta w}$	Instantaneous constant of HBm
p_f	Pore fluid pressure
p_{w_MC}	Mud pressure calculated with M-C (plateau)
p_{w_slip}	Mud pressure calculated with WPM
$p_{w\_H\&Bm}$	Mud pressure calculated with HBm
$R = \sigma_{MAX}/\sigma_{min}$	Ratio of the far field stresses
S	Induced tangential stress at the wellbore boundary
S_z	Induced axial stress at the wellbore boundary
β_w	Angle between the maximum principal stress and the normal to the weakness plane
δ	Inclination of the weakness planes in the wellbore cross section (clockwise from σ_{MAX})
δ^*	Inclination of the weakness planes in the wellbore cross section (clockwise from σ_{MAX}) in the rotated reference system
δ_{crit}	Critical inclination for slip
ϕ'_w	Friction angle of the weakness planes
ϕ'	Friction angle of the rock matrix
ϑ	Wellbore azimuth
σ_c	Uniaxial compressive strength of the rock matrix
$\sigma_{c\beta w}$	Instantaneous uniaxial compressive strength (HBm)
σ_z	Far field stress in the direction of the borehole axis (principal stress)
σ_{MAX}	Maximum far field stress (principal stress)
σ_{min}	Minimum in situ stress (principal stress)
σ'_θ	Effective tangential stress
σ'_r	Effective radial stress
σ'_1	Maximum effective principal stress
σ'_3	Minimum effective principal stress

References

1. Boggs, S. *Petrology of Sedimentary Rocks*; Cambridge university press: Cambridge, UK, 2009
2. Carey, J.W.; Torsæter, M. Shale and Wellbore Integrity. In *Shale: Subsurface Science and Engineering*; John Wiley & Sons: Hoboken, NJ, USA, 2019; pp. 145–159.
3. Steiger, R.P.; Leung, P.K. Quantitative determination of the mechanical properties of shales. *SPE Drill. Drill. Eng.* **1992**, *7*, 181–185.
4. Peter, A.; Yang, D.; Eshiet, K.I.I.I.; Sheng, Y. A Review of the Studies on CO2–Brine–Rock Interaction in Geological Storage Process. *Geosciences* **2022**, *12*, 168.
5. Benlalam, N.; Serazio, C.; Rocca, V. VEM application to geomechanical simulations of an Italian Adriatic offshore gas storage scenario. *GEAM* **2022**, *165*, 41–49.
6. Benetatos, C.; Rocca, V.; Verga, F.; Adinolfi, L.; Marzano, F. Deformation behavior of a regional shale formation from integrated laboratory and well data analysis: Insights for underground fluid storage in northern Italy. *Geoenergy Sci. Eng.* **2023**, *229*, 212109.
7. Benetatos, C.; Bocchini, S.; Carpignano, A.; Chiodoni, A.; Cocuzza, M.; Deangeli, C.; Eid, C.; Ferrero, D.; Gerboni, R.; Giglio, G.; et al. How underground systems can contribute to meet the challenges of energy transition. *Geam. Geoing. Ambient. E Mineraria* **2021**, *58*, 65–80.
8. Pašić, B; Gaurina-Međimurec, N.; Mijić; P; Medved, I. Experimental research of shale pellet swelling in nano-based drilling muds. *Energies* **2020**, *13*, 6246.

9. Ambati, V.; Mahadasu, N.B.; Nair, R.R. Reservoir wellbore stability analysis and weak zones identification using the 1d mem, swelling tests and ucs: A case study from mumbai offshore, India. *Arab. J. Sci. Eng.* **2021**, *47*, 11101–11123.
10. Blkoor, S.O.; Norddin, M.N.A.B.M.; Ismail, I.; Oseh, J.O.; Basaleh, S.S.; Bin Risal, A.R.; Bin Sariman, M.F.; Ngouangna, E.N. Enhancing the stability of shale in water-based fluid with polyethylene glycol/nanosilica composite grafted with sodium dodecyl sulfate. *Arab. J. Geosci.* **2023**, *16*, 541.
11. Zhang, F.; Liu, H.; Meng, Y.; Cui, S.; Ye, H. Study on Wellbore Stability and Failure Regions of Shale considering the Anisotropy of Wellbore Seepage. *Geofluids* **2021**, *2021*, 6694689.
12. Ma, T.; Wang, H.; Liu, Y.; Shi, Y.; Ranjith, P.G. Fracture-initiation pressure model of inclined wells in transversely isotropic formation with anisotropic tensile strength. *Int. J. Rock Mech. Min. Sci.* **2022**, *159*, 105235.
13. Zhang, F.; Liu, H.B.; Cui, S.; Meng, Y.F.; Wang, J.J. Influence of the weakening effect of drilling fluid on wellbore stability in anisotropic shale formation. *Front. Phys.* **2021**, *9*, 745075.
14. Ding, L.; Wang, Z.; Lv, J.; Wang, Y.; Liu, B. A New Model for Real-Time Prediction of Wellbore Stability Considering Elastic and Strength Anisotropy of Bedding Formation. *Energies* **2021**, *15*, 251.
15. Shang, X.; Zhang, Z. Elastic-plastic-damaged zones around a deep circular wellbore under non-uniform loading. *Symmetry* **2020**, *12*, 323.
16. Medved, I.; Gaurina-Međimurec, N.; Pašić, B; Mijić, P. Green approach in water-based drilling mud design to increase wellbore stability. *Appl. Sci.* **2022**, *12*, 5348.
17. Mehrabian, A.; Nguyen, V.X.; Abousleiman, Y.N. Wellbore mechanics and stability in shale. In *Shale: Subsurface Science and Engineering*; John Wiley & Sons: Hoboken, NJ, USA, 2019; pp. 197–212.
18. Deangeli, C.; Marchelli, M. Combined Effect of Pore Water Overpressure, Far-Field Stresses, and Strength Parameters in Wellbore Stability. *Front. Earth Sci.* **2022**, *10*, 860818.
19. Basu, S.; Jones, A.; Mahzari, P. Best practices for shale core handling: Transportation, sampling and storage for conduction of analyses. *J. Mar. Sci. Eng.* **2020**, *8*, 136.
20. Josh, M.; Esteban, L.; Delle Piane, C.; Sarout, J.; Dewhurst, D.N.; Clennell, M.B. Laboratory characterisation of shale properties. *J. Pet. Sci. Eng.* **2012**, *88*, 107–124.
21. Risnes, R. Deformation and yield in high porosity outcrop chalk. *Phys. Chem. Earth Part A: Solid Earth Geod.* **2001**, *26*, 53–57.
22. Abousleiman, Y.; Tran, M.; Hoang, S.; Bobko, C.; Ortega, A.; Ulm, F.J. Geomechanics field and laboratory characterization of Woodford shale: The next gas play. In *SPE Annual Technical Conference and Exhibition?* SPE: Calgary, AB, Canada, 2007 ;p. SPE-110120.
23. Woehrl, B.; Wessling, S.; Bartetzko, A.; Pei, J.; Renner, J. Comparison of methods to derive rock mechanical properties from formation evaluation logs. In *ARMA US Rock Mechanics/Geomechanics Symposium*; ARMA: Palo Alto, CA, USA, 2010; p. ARMA-10. .
24. Mandal, P.P.; Essa, I.; Saha, S.; Rezaee, R. Multi-Purpose Utility of Constructing 3D Static Geomechanical Model in the Ichthys Field, Browse Basin. In Proceedings of the Australian Exploration Geoscience Conference AEGC, Brisbane, Australia, 15–20 September 20212021
25. Chang, C.; Zoback, M.D.; Khaksar, A. Empirical relations between rock strength and physical properties in sedimentary rocks. *J. Pet. Sci. Eng.* **2006**, *51*, 223–237.
26. Khaksar, A.; Taylor, P.G.; Fang, Z.; Kayes, T.; Salazar, A.; Rahman, K. Rock strength from core and logs, where we stand and ways to go. In *SPE Europec featured at EAGE Conference and Exhibition?* SPE: Calgary, AB, Canada, 2009; p. SPE-121972.
27. Zhang, J.J. *Applied Petroleum Geomechanics*; Gulf Professional Publishing: Cambridge, MA, USA, Imprint of Elsevier: Amsterdam, The Netherlands, 2019. https://doi.org/10.1016/C2017-0-01969-9.
28. Miah, M.I.; Ahmed, S.; Zendehboudi, S.; Butt, S. Machine learning approach to model rock strength: Prediction and variable selection with aid of log data. *Rock Mech. Rock Eng.* **2020**, *53*, 4691–4715.
29. Shao, Z.; Armaghani, D.J.; Bejarbaneh, B.Y.; Mu'azu, M.A.; Mohamad, E.T. Estimating the friction angle of black shale core specimens with hybrid-ANN approaches. *Measurement* **2019**, *145*, 744–755.
30. Horsrud, P. Estimating Mechanical Properties of Shale From Empirical Correlations. *J. SPE Drill. Complet.* **2001**, *16*, 68–73. https://doi.org/10. 2118/56017-pa.
31. Van Oort, E. On the physical and chemical stability of shales. *J. Pet. Sci. Eng.* **2003**, *38*, 213–235.
32. Wasantha, P.L.; Ranjith, P.G. Water-weakening behavior of Hawkesbury sandstone in brittle regime. *Eng. Geol.* **2014**, *178*, 91–101.
33. Liu, W.; Yang, K.; Zhang, S.; Zhang, Z.; Xu, R. Energy evolution and water immersion-induced weakening in sandstone roof of coal mines. *Int. J. Coal Sci. Technol.* **2022**, *9*, 53.
34. Jingyuan, M.; Boru, X.; Yuxiu, A. Advanced developments in low-toxic and environmentally friendly shale inhibitor: A review. *J. Pet. Sci. Eng.* **2022**, *208*, 109578.
35. Valès, F.; Minh, D.N.; Gharbi, H.; Rejeb, A. Experimental study of the influence of the degree of saturation on physical and mechanical properties in Tournemire shale (France). *Appl. Clay Sci.* **2004**, *26*, 197–207.
36. Asaka, M.; Holt, R.M. Anisotropic wellbore stability analysis: Impact on failure prediction. *Rock Mech. Rock Eng.* **2021**, *54*, 583–605.
37. Aoki, T.; Tan, C.P.; Bamford, W.E. Effects of deformation and strength anisotropy on borehole failures in saturated shales. *Int. J. Rock Mech. Min. Sci. Geomech. Abstr. UK* 1993, *30*, 7031865.

38. Detournay, E.; Atkinson, C. Influence of pore pressure on the drilling response in low-permeability shear-dilatant rocks. *Int. J. Rock Mech. Min. Sci.* **2000**, *37*, 1091–1101.
39. Tran, N.H.; Do, D.P.; Vu, M.N.; Nguyen, T.T.N.; Pham, D.T.; Trieu, H.T. Combined effect of anisotropy and uncertainty on the safe mud pressure window of horizontal wellbore drilled in anisotropic saturated rock. *Int. J. Rock Mech. Min. Sci.* **2022**, *152*, 105061.
40. Abdi, H.; Labrie, D.; Nguyen, T.; Barnichon, J.; Su, G.; Evgin, E.; Simon, R.; Fall, M. Laboratory investigation on the mechanical behaviour of Tournemire argillite. *Can. Geotech. J.* **2015**, *52*, 268–282.
41. Jaeger, J. C. Shear failure of anisotropic rocks. *Geol. Mag.* **1960**, *97*, 65–72.
42. Hoek, E.; Brown, E.T. Empirical strength criterion for rock masses. *J. Geotech. Geoenv. Eng.* **1980**, *106*, 1013–1035.
43. Hoek, E.; Brown, E.T. The Hoek–Brown failure criterion and GSI–2018 edition. *J. Rock Mech. Geotech. Eng.* **2019**, *11*, 445–463.
44. Terzaghi, K. The Shearing Resistance of Saturated Soils and the Angle between the Planes of Shear. *First Int. Conf. Soil Mech. Found. Eng.* **1936**, *1*, 54–56.
45. Detournay, E.; Cheng, A.H.-D. Fundamentals of Poroelasticity. *Anal. Des. Methods Pergamon* **1993**, *5*, 113–171. https://doi.org/10.1016/b978-0-08- 040615-2.50011-3.
46. Fjaer, E.; Holt, R.M.; Raaen, A.M.; Risnes, R.; Horsrud, P. *Petroleum Related Rock Mechanics*, 2nd ed.; Elsevier: Oxford, UK, 2008.
47. Brady, B.; Brown, E. *Rock Mechanics for Underground Mining*; Kluwer academic Publishers: Dorrecht, The Netherlands; Boston, MA, USA; London, UK, 2004.
48. Tien, Y.M.; Kuo, M.C.; Juang, C.H. An experimental investigation of the failure mechanism of simulated transversely isotropic rocks. *Int. J. Rock Mech. Min. Sci.* **2006**, *43*, 1163–1181.
49. Hoek, E.; Brown, E.T. *Underground Excavations in Rock*; CRC Press: London, UK, 1980; 527p. https://doi.org/10.1201/9781482288926.
50. Tien, Y.M.; Kuo, M.C. A failure criterion for transversely isotropic rocks. *Int. J. Rock Mech. Min. Sci.* **2001**, *38*, 399–412.
51. Colak, K.; Unlu, T. Effect of transverse anisotropy on the Hoek–Brown strength parameter 'mi' for intact rocks. *Int. J. Rock Mech. Min. Sci.* **2004**, *41*, 1045–1052.
52. Deangeli, C.; Omwanghe, O.O. Prediction of mud pressures for the stability of wellbores drilled in transversely isotropic rocks. *Energies* **2018**, *11*, 1944.
53. Deangeli, C.; Cardu, M.; Martinelli, D. Analysis of the Stability of Openings Excavated in Anisotropic Rocks. In *Challenges and Innovations in Geomechanics, Proceedings of the 16th International Conference of IACMAG, Turin, Italy, 30 August–2 September 2022*; Lecture Notes in Civil Engineering 126; Springer International Publishing: Berlin/Heidelberg, Germany, 2021; Volume 216, pp. 361–368
54. Parkash, D. Deangeli, C. Wellbore stability analysis in anisotropic shale formations. In Proceedings of the Society of Petroleum Engineers—SPE/PAPG Pakistan Section Annual Technical Symposium and Exhibition 2019, PATS 2019, Islamabad, Pakistan, 18–19 November 2019; p. SPE-201183.
55. Ma, T.; Wu, B.; Fu, J.; Zhang, Q.; Chen, P. Fracture pressure prediction for layered formations with anisotropic rock strengths. *J. Nat. Gas Sci. Eng.* **2017**, *38*, 485–503.
56. Ma, T.; Zhang, Q.B.; Chen, P.; Yang, C.; Zhao, J. Fracture pressure model for inclined wells in layered formations with anisotropic rock strengths. *J. Pet. Sci. Eng.* **2017**, *149*, 393–408.
57. Ma, T.; Peng, N.; Zhu, Z.; Zhang, Q.; Yang, C.; Zhao, J. Brazilian Tensile Strength of Anisotropic Rocks: Review and New Insights. *Energies* **2018**, *11*, 304.
58. De Gennaro, V.; Amri, R.; Brignoli, M.; Kallel, N.; Wielemaker, E.; El Ayeb, S. Integrated unconventional gas evaluation workflow: From anisotropic geomechanical modelling to completion design. In *SPE/EAGE European Unconventional Resources Conference and Exhibition*; European Association of Geoscientists & Engineers: Unnik, The Netherlands, 2014; Volume 2014, pp. 1–16
59. Deangeli, C. Failure in the tension zone around a circular tunnel excavated in saturated porous rock. *Appl. Sci.* **2021**, *11*, 8384.
60. Perras, M.A.; Diederichs, M.S. A review of the tensile strength of rock: Concepts and testing. *Geotech. Geol. Eng.* **2014**, *32*, 525–546.
61. Hoek, E. *Practical Rock Engineering*; Rocscience Inc.: Toronto, ON, Canada, 2006
62. Hoek, E. Estimating Mohr-Coulomb friction and cohesion values from the Hoek-Brown failure criterion. In *International Journal of Rock Mechanics and Mining Sciences & Geomechanics* Abstracts; Elsevier BV: Amsterdam, The Netherlands, 1990; Volume 27, pp. 227–229.
63. He, S.; Wang, W.; Zhou, J.; Huang, Z.; Tang, M. A model for analysis of wellbore stability considering the effects of weak bedding planes. *J. Nat. Gas Sci. Eng.* **2015**, *27*, 1050–1062.
64. Kanfar, M.F.; Chen, Z.; Rahman, S.S. Risk-controlled wellbore stability analysis in anisotropic formations. *J. Pet. Sci. Eng.* **2015**, *134*, 214–222.
65. Zhang, M.; Fan, X.; Zhang, Q.; Yang, B.; Zhao, P.; Yao, B.; He, L. Influence of multi-planes of weakness on unstable zones near wellbore wall in a fractured formation. *J. Nat. Gas Sci. Eng.* **2021**, *93*, 104026.
66. Qiu, Y.; Ma, T.; Peng, N.; Liu, Y.; Liu, J.; Ranjith, P.G. Wellbore stability analysis of inclined wells in transversely isotropic formations accounting for hydraulic-mechanical coupling. *Geoenergy Sci. Eng.* **2023**, *224*, 211615.
67. Fan, X.; Zhang, M.; Zhang, Q.; Zhao, P.; Yao, B.; Lv, D. Wellbore stability and failure regions analysis of shale formation accounting for weak bedding planes in ordos basin. *J. Nat. Gas Sci. Eng.* **2020**, *77*, 103258.

68. Li, Y.; Weijermars, R. Wellbore stability analysis in transverse isotropic shales with anisotropic failure criteria. *J. Pet. Sci. Eng.* **2019**, *176*, 982–993.